

# Extending the Range of Nitrofurantoin Solid Forms: Effect of Molecular and Crystal Structure on Formation Thermodynamics and Physicochemical Properties

Published as part of a *Crystal Growth and Design* joint virtual special issue on *Crystallizing the Role of Solid-State Form in Drug Delivery*

Artem O. Surov, Alexander P. Voronin, Ksenia V. Drozd, Tatyana V. Volkova, Nikita Vasilev, Dmitriy Batov, Andrei V. Churakov, and German L. Perlovich\*



Cite This: <https://doi.org/10.1021/acs.cgd.2c00044>



Read Online

ACCESS |



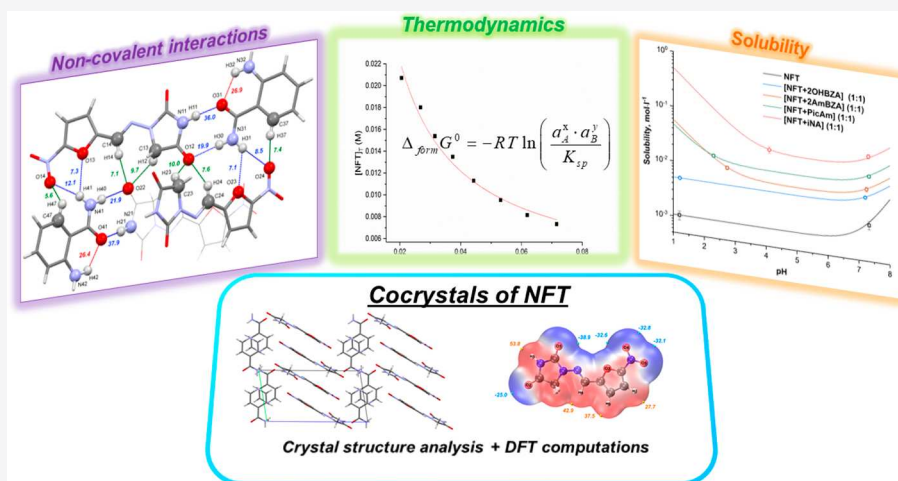
Metrics & More



Article Recommendations



Supporting Information



**ABSTRACT:** In this work, four novel pharmaceutical cocrystals of nitrofurantoin, an antibacterial drug, with isonicotinamide, picolinamide, 2-hydroxybenzamide, and 2-aminobenzamide have been obtained and thoroughly characterized by various analytical techniques. The crystal structures of the solid forms have been elucidated by single-crystal X-ray diffraction, and the energy distribution of intermolecular interactions has been further quantified on the basis of QTAIMC analysis. Eight distinct supramolecular heterosynthons of hydrogen bonding have been identified in the studied crystals, and their relative stability has been ranked in terms of total interaction energies. The thermodynamics of the cocrystallization reactions has been systematically investigated using two independent experimental techniques, namely solution calorimetry and phase solubility diagram, which allowed us to assess both the enthalpic and the entropic contributions to the cocrystal formation driving force. The pH-solubility behavior of the cocrystals has been investigated at different pH values using eutectic concentrations of the components. Although all of the cocrystals reported here were found to be more soluble than the parent drug, their advantage in thermodynamic solubility did not translate into enhanced dissolution performance due to a rapid solution-mediated phase transformation in aqueous media. In addition, the effect of cocrystallization on other pharmaceutically relevant properties of nitrofurantoin, including photostability and membrane permeability, has been considered and analyzed.

## 1. INTRODUCTION

Pharmaceutical cocrystallization has been proven to be a potent approach toward modification, control, and fine tuning of the most pharmaceutically critical properties, including solubility, dissolution rate, stability, bioavailability, mechanical strength, and permeability of active pharmaceutical ingredients (APIs), without changing their pharmacophore structure.<sup>1–6</sup> This approach has recently become an integral part of contemporary

Received: January 12, 2022

Revised: March 2, 2022

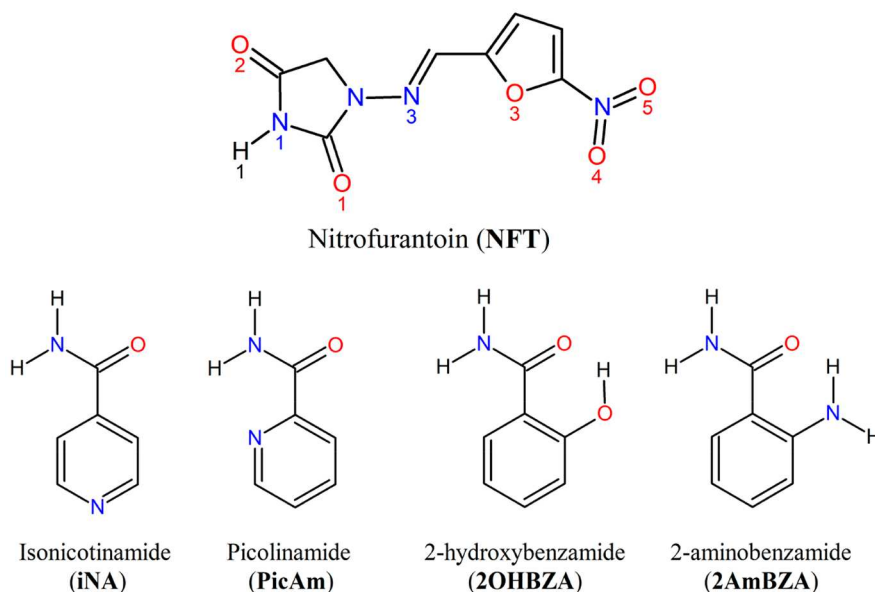


**Figure 1.** Molecular structures of nitrofurantoin and the coformers used in this work.

drug solid form design.<sup>7,8</sup> The great success of the cocrystallization strategy highlighted by numerous academic investigations has provided compelling evidence for the industrial community and regulatory authorities that cocrystals should be considered valuable and competitive pharmaceutical products. As a result, currently, several drugs formulated as cocrystals are available on the market.<sup>1,9</sup>

Structurally, the deliberate design of multicomponent crystals relies on the concept of supramolecular synthons,<sup>10–12</sup> which are defined as spatial arrangements of intermolecular interactions<sup>13</sup> that occur in a repeatable and predictable fashion, regardless of the availability of other functional groups.<sup>14</sup> The identification and understanding of appropriate intermolecular interactions that govern and control molecular assembly through supramolecular synthons are the basis of crystal engineering.<sup>15–17</sup> Thermodynamically, a favorable and spontaneous cocrystallization reaction is associated with the negative values of the Gibbs energy change ( $\Delta_{\text{form}}G^\circ$ ), so that the stability of the resulting multicomponent phase relative to its precursors increases as the Gibbs energy becomes more negative.<sup>18–20</sup> Since  $\Delta_{\text{form}}G^\circ$  includes enthalpic and entropic components, a fundamental understanding of the cocrystal thermodynamic stability seems incomplete without taking into account the relative contributions of each of these terms to the driving force of the cocrystallization process. Although computational studies consistently predict that the formation of most organic binary crystal systems is controlled by the enthalpy term and originates from the lattice energy gain due to new or more effective intermolecular contacts,<sup>21,22</sup> sparse experimental data indicate that entropically favorable cocrystals are not exceptionally rare and presumably constitute a notable part of cocrystallization outcomes.<sup>23–25</sup> In fact, according to a recent theoretical study by Perlovich, the fraction of such systems is expected to be about 30%.<sup>26</sup> However, it is still challenging to rationalize the structure–energy relationships in multicomponent crystals mainly because the entropic contribution and thermal effects in the computational works are normally neglected and there is not enough reliable experimental thermodynamic information in the literature.

The objects of the present work are pharmaceutical cocrystals of nitrofurantoin (NFT), an antibacterial drug (Figure 1), which is included in the WHO Model List of Essential Medicines and is widely used to treat urinary tract infections.<sup>27</sup> Nitrofurantoin is a derivative of imidazolidinedione, and the same principal cyclic imide fragment (imidazolidine-2,4-dione or pyrrolidine-2,5-dione) can be observed in such drugs as dantrolene,<sup>28</sup> 5-fluorouracil,<sup>29</sup> lenalidomide,<sup>30</sup> tegafur,<sup>31</sup> sofosbuvir,<sup>32</sup> and zidovudine.<sup>33</sup> According to several literature sources,<sup>34–36</sup> nitrofurantoin belongs to class IV of the Biopharmaceutics Classification System (BCS),<sup>37</sup> which indicates its low aqueous solubility and insufficient permeability. Due to the poor solubility and permeability of NFT, its bioavailability attains only values of 20–30%.<sup>38,39</sup> There have been a number of attempts to address the poor physicochemical performance of the drug by applying the cocrystallization approach. An extensive set of multicomponent solid forms of NFT, including cocrystals, solvates, and salts, have been obtained and investigated by Vangala et al.<sup>40–42</sup> In particular, the authors showed that NFT cocrystallization with 4-hydroxybenzoic acid and 4-hydroxybenzamide resulted in a substantial improvement in the drug photostability and enhancement of its dissolution rate.<sup>40,41</sup> The pharmaceutical cocrystal of NFT with 4-aminobenzoic acid with superior dissolution characteristics has been described by Cherukuvada et al.<sup>34</sup> Screening, structural analysis, and investigation of the solution stability of NFT cocrystals with a range of pharmaceutically relevant coformers have been reported by Alhalaweh et al.<sup>43</sup> In addition, binary drug–drug solid forms of NFT with trimethoprim have been developed to overcome the drawbacks related to fixed-dose drug combinations and exhibited greater antibacterial activity *in vivo*, in comparison to the parent compounds.<sup>36</sup>

In this work, we have extended the existing set of NFT multicomponent crystals by forming novel pharmaceutical cocrystals with structurally related carboxamide compounds (isonicotinamide, picolinamide, 2-hydroxybenzamide, and 2-aminobenzamide). The crystal structures of the obtained solid forms were elucidated by single-crystal X-ray diffraction, and the energy distribution of intermolecular interactions was further quantified on the basis of QTAIMC analysis. The thermody-

namics of the cocrystallization reactions was thoroughly investigated using two independent experimental techniques, namely solution calorimetry and phase solubility diagram, which allowed us to determine both the enthalpic and entropic contributions to the cocrystal formation driving force. The pH-solubility behavior of the cocrystals was investigated at different pH values using eutectic concentrations of the components. Even though all of the cocrystals reported here were found to be more soluble than the parent drug, their advantage in thermodynamic solubility did not translate into an enhanced dissolution performance due to a rapid solution-mediated phase transformation in aqueous media. In addition, the effect of cocrystallization on other pharmaceutically relevant properties of NFT, including photostability and membrane permeability, was considered and analyzed.

## 2. MATERIALS AND METHODS

**2.1. Compounds and Solvents.** Nitrofurantoin was purchased from Acros Organics and corresponded to polymorphic form  $\beta$  of this drug, as verified by the Cambridge Structural Database (CSD) code: LABJON02. All the cofomers were purchased from Sigma-Aldrich. The materials were used as received. The solvents were of analytical or chromatographic grade.

**2.2. Mechanochemical Experiments.** The grinding experiments were performed using a Fritsch planetary micro mill, Model Pulverisette 7, in 12 mL agate grinding jars with 10 5 mm agate balls at a rate of 500 rpm for 60 min. In a typical experiment, 50–60 mg of a physical mixture of NFT and a cofomer in a 1:1 molar ratio were placed into a grinding jar, and 50  $\mu$ L of acetonitrile was added with a micropipet. The resulting powder samples were analyzed by PXRD and DSC.

**2.3. Solution Crystallization.** The single crystals of NFT cocrystals were synthesized using the slow evaporation method from acetonitrile as a solvent. Initially, the solubility of NFT and the cofomers used was determined by the gravimetric method. In brief, a slurry containing each substance was stirred for 48 h in 2 mL of acetonitrile. The slurry was filtered using a Rotilabo PTFE syringe filter with 0.2  $\mu$ m pores into preweighed vials and left until evaporation was complete. The vials were reweighed after drying, and the solubility of the compounds was estimated. These preliminary results prompted us to use an excess of the corresponding cofomer in the solution crystallization experiments. In a typical experiment, physical mixtures (40–80 mg) with the NFT-cofomer molar ratios from 1:1 to 1:10 were dissolved in acetonitrile. The resulting solutions were filtered into 10 mL vials, covered by Parafilm perforated with a few small holes, and allowed to evaporate slowly in the dark at room temperature until a crystalline material was formed. Good quality single crystals of NFT with iNA, later identified as [NFT-iNA] (1:1) cocrystal, were obtained from the acetonitrile solution with a 1:1 molar ratio of the components. Single crystals of NFT with 2OHBZA, PicAm, and 2AmBZA, identified as [NFT-2OHBZA] (1:1), [NFT-PicAm] (1:1), and [NFT-2AmBZA] (1:1) cocrystals, were obtained from acetonitrile solutions with 1:10 or 1:5 molar ratios of the components, respectively.

**2.4. Single-Crystal XRD.** The single-crystal diffraction data for the NFT cocrystals were collected using a Bruker SMART APEX II diffractometer (Bruker AXS, Germany) with graphite-monochromated Mo K $\alpha$  radiation ( $\lambda = 0.71073$  Å). Absorption corrections based on measurements of equivalent reflections were applied.<sup>44</sup> The structures were solved by direct methods and refined by full-matrix least-squares on  $F^2$  with anisotropic thermal parameters for all of the non-hydrogen atoms.<sup>45</sup> All of the hydrogen atoms were found from the difference Fourier maps and refined isotropically. The crystallographic data were deposited with the Cambridge Crystallographic Data Centre as supplementary publications under the CCDC numbers 2131165–2131168. This information can be obtained free of charge from the Cambridge Crystallographic Data Centre at [www.ccdc.cam.ac.uk/data\\_request/cif](http://www.ccdc.cam.ac.uk/data_request/cif).

**2.5. Powder X-ray Diffraction (PXRD).** The laboratory PXRD data of the bulk materials were recorded under ambient conditions on a

D2 Phaser (Bragg–Brentano) diffractometer (Bruker AXS, Germany) with a copper X-ray source ( $\lambda_{\text{CuK}\alpha 1} = 1.5406$  Å) and a LYNXEYE XE-T high-resolution position-sensitive detector. The samples were placed into the plate sample holders and rotated at a rate of 15 rpm during the data acquisition.

**2.6. Thermal Analysis.** **2.6.1. DSC.** The thermal analysis was carried out using a differential scanning calorimeter with a refrigerated cooling system (PerkinElmer DSC 4000, USA). The sample was heated in a sealed aluminum sample holder at a rate of 10 °C min<sup>-1</sup> under a nitrogen atmosphere. The unit was calibrated by indium and zinc standards. The accuracy of the weighing procedure was  $\pm 0.01$  mg.

**2.6.2. TGA.** TGA was performed on a TG 209 F1 Iris thermomicrobalance (Netzsch, Germany). Approximately 10 mg of the sample was placed in a platinum crucible. The samples were heated at a constant heating rate of 10 °C min<sup>-1</sup> and purged with a dry argon stream at a rate of 30 mL min<sup>-1</sup> throughout the experiment.

**2.7. Solubility Experiments.** **2.7.1. Solubility in Acetonitrile and Phase Diagram Construction.** The solubility measurements of NFT, iNA, PicAm, 2OHBZA, 2AmBZA, and the respective cocrystals were made with a ThermoMixer C instrument (Eppendorf, Hamburg, Germany) with continuous shaking (1000 rpm) for 72 h at  $25.0 \pm 0.1$  °C. An excess of each solid was placed into Eppendorf tubes, and 1 mL of acetonitrile was added. After 48 h of shaking, the suspension was allowed to settle for 1 h and was filtered using a Rotilabo PTFE syringe filter with 0.2  $\mu$ m pores. The sample was diluted by the mobile phase, and the concentration of each compound in the saturated solution was analyzed by HPLC. The solubility of the NFT cocrystals in cofomer acetonitrile solutions was determined by the same methods as described above. Cofomer solutions were prepared by diluting stock solutions of each cofomer with acetonitrile. The solid phases after the experiment were dried and examined by PXRD. The results are stated as the average of at least three replicated experiments.

**2.7.2. Aqueous Solubility.** The saturation shake-flask method was also used to estimate the thermodynamic solubility of NFT and to determine the eutectic concentrations of the cocrystal components in aqueous solutions with pH 1.2 and 7.4 at  $37.0 \pm 0.1$  °C. In a typical experiment, 30 mg (0.126 mmol) of NFT and 80–120 mg of the cocrystal were suspended in 2 mL of the buffer solution and shaken at 37 °C for 72 h in order to reach the eutectic point between the drug and the cocrystal. After the equilibration, the suspension was allowed to settle for 1 h and the equilibrium pH of each solution was measured (pH-meter FG2, Mettler Toledo). The saturated solutions were filtered using a Rotilabo PTFE syringe filter with 0.2  $\mu$ m pores and diluted by a mobile phase, and the concentration of each compound in the eutectic point was analyzed by HPLC. The results are stated as the average of at least three replicated experiments. A PXRD analysis was performed to confirm that the samples represented a mixture of two solid phases: NFT and the cocrystal.

**2.8. Dissolution Studies.** The powder dissolution experiments were carried out by the paddle method using a USP-certified Electrolab EDT-08LX dissolution tester applying the USP II paddle method for 360 min. Approximately 215 mg (0.903 mmol) of pure NFT or an NFT-equivalent amount of the cocrystals (nonsink conditions) was added to 300 mL of a pH 7.4 buffer solution with a paddle speed of 100 rpm at  $37.0 \pm 0.1$  °C. Aliquots of the suspension were withdrawn at certain time intervals, and an equal volume of a fresh medium was added to maintain a constant dissolution medium volume. The samples were filtered using a Rotilabo PTFE syringe filter with 0.2  $\mu$ m pores. The drug content and cofomer concentration in the solution phase were determined after suitable dilution by HPLC. The results are stated as the average of three replicated experiments. The solution pH was measured at the beginning and at the end of each dissolution experiment. The percentage of the cocrystal dissolved was calculated according to

$$\begin{aligned} & \text{cocrystal dissolved (\%)} \\ &= 100 \times (\text{moles of cofomer dissolved} \\ & \quad / \text{initial moles of cocrystal added}) \end{aligned} \quad (1)$$

The second dissolution test was carried out by the USP I basket method for 360 min. The cylindrical tablets were prepared by direct compression of NFT or an NFT-equivalent amount of the cocrystals (the same amount of the samples as for powder dissolution was used), using a laboratory press fitted with a 10 mm flat-faced punch and a die set, applying a force of 3 tons for about 5 min. The dissolution medium volume was 400 mL of the pH 7.4 buffer solution with a stirring speed of 150 rpm at  $37.0 \pm 0.1$  °C for 360 min. At predefined time intervals, 1 mL of the dissolution medium was withdrawn and replaced with an equal volume of fresh medium to maintain a constant volume. The samples were filtered and diluted properly to determine the concentrations of NFT and the cofomers by HPLC. After the dissolution experiments, the solid residues were collected and dried at room temperature for PXRD analysis.

**2.9. Diffusion Studies.** The diffusion studies of NFT and its cocrystals were performed in a vertical type Franz diffusion cell (PermeGear, Inc., Hellertown, PA, USA) with a 7 mL volume through a Permeapad TM barrier (PHABIOC shop, Fritz-Souchon-Str. 27, 32339 Espelkamp, Germany). The barrier was mounted between the donor (lower) and the receptor (upper) compartments. The effective surface area for the permeation process was 0.785 cm<sup>2</sup>. The donor compartment containing roughly 5.0 mg of NFT or an equivalent amount of the cocrystals was filled with 7 mL of a pH 7.4 aqueous solution and was stirred magnetically at 500 rpm. The acceptor compartment was filled with 1 mL of pure pH 7.4 aqueous solution. The temperature in the diffusion cell apparatus was maintained at  $37.0 \pm 0.1$  °C. Samples (0.5 mL) were withdrawn at definite time intervals and were analyzed by HPLC.

**2.10. Photostability.** The photostability studies were carried out using a Elektronika UFO-B-04 (Russia) UV floodlight at room temperature. The wavelength of the artificial UV light was between 200 and 400 nm. The powder samples of NFT and its cocrystals were sieved by 60 mesh sieves (250 μm) and exposed to UV irradiation. After certain time intervals (1, 2, 4, 10, 25, 40, and 60 h), a sample of the solid was taken, and the nondegraded NFT amount was analyzed by HPLC.

**2.11. High-Performance Liquid Chromatography (HPLC).** HPLC was performed on a LC-20 AD Shimadzu Prominence model equipped with a PDA detector and a Luna C-18 column (150 mm × 4.6 mm i.d., 5 μm particle size, and 100 Å pore size). The column temperature was set to 40 °C. The elution of the samples was achieved by a mobile phase consisting of acetonitrile and a 0.1% aqueous solution of trifluoroacetic acid mixed in a 15:85 ratio (v:v) in the isocratic regime at a flow rate of 1 mL min<sup>-1</sup>. The injection volume was 20 μL. The UV detection of nitrofurantoin, isonicotinamide, picolinamide, 2-hydroxybenzamide and 2-aminobenzamide was carried out at the wavelengths 265, 263, 265, 300, and 321 nm, respectively.

**2.12. Solution Calorimetry.** The enthalpies of dissolution of the solid forms were measured at  $25.00 \pm 0.001$  °C using an automated isoperibol ampule-type calorimeter fitted with a 30 cm<sup>3</sup> titanium vessel. The detection limit of the apparatus was  $\delta T = 10^{-5}$  K, and the temperature instability in the bath was  $\delta T = 10^{-3}$  K in the temperature range considered. All of the experiments were performed in neat acetonitrile or acetonitrile solutions of the cofomers, as all solids dissolved well with a large endothermic heat effect in this solvent. The dissolution enthalpies ( $\Delta_{\text{sol}}H_{\text{m}}$ ) were independent of the solute molality (mol kg<sup>-1</sup>) in the investigated concentration range; therefore, the standard enthalpy of dissolution ( $\Delta_{\text{sol}}H^{\circ}$ ) was equal to the mean value of the experimental  $\Delta_{\text{sol}}H_{\text{m}}$  values. The experimental procedure of  $\Delta_{\text{sol}}H_{\text{m}}$  measurements and instrument calibration has been detailed elsewhere.<sup>46–48</sup>

**2.13. Computational Methods.** **2.13.1. Periodic DFT Calculations.** The periodic DFT computations with localized Gaussian basis sets were performed using CRYSTAL17 software<sup>49</sup> at the B3LYP-D3(BJ,ABC)/6-31G(d,p) level of theory.<sup>50–52</sup> It was demonstrated that this level of theory provided reliable and consistent results when the noncovalent interactions in organic crystals were studied.<sup>53</sup> The unit cell parameters of the crystals obtained in the X-ray diffraction experiment were fixed, and the structural relaxations were limited to the positional parameters of the atoms. An experimental crystal structure

with normalized X–H bond lengths was used as the starting point for geometry optimization. The shrinking factor reflecting the density of the *k*-points grid in the reciprocal space was set to at least 4 depending on the reciprocal lattice vectors in a particular crystal. The TOLDEE and TOLINTEG parameters were set to 10 and 777725, respectively. All the normal vibrational modes for the relaxed structures were found to have positive frequencies, which is an indicator of the local minimum on the potential energy surface. Further computational details had been described in our previous works.<sup>54,55</sup>

**2.13.2. Noncovalent Interaction Energies and Lattice Energy Calculation.** In order to quantify the energies of particular noncovalent interactions in the crystal, a Bader analysis of periodic electron density in the crystal (or QTAIMC) was performed with the TOPOND software<sup>56</sup> currently built into the CRYSTAL suite. The search for (3;–1) critical points was conducted between pairs of atoms within the 5 Å radius, and the interactions with positive Laplacian and electron density,  $\rho_{\text{b}}$ , at the (3;–1) point higher than 0.003 au were taken into consideration.

The energy of a particular noncovalent interaction,  $E_{\text{int}}$ , was evaluated on the basis of the local kinetic energy density at the (3;–1) critical point ( $G_{\text{b}}$ ) by the correlation equation proposed in the work by Mata et al.<sup>57</sup>

$$E_{\text{int}} \text{ (kJ mol}^{-1}\text{)} = 1147 \times G_{\text{b}} \text{ (au)} \quad (2)$$

Equation 2 yields reasonable  $E_{\text{int}}$  values for molecular crystals with different types of intermolecular interactions, including conventional and nonconventional hydrogen bonds, halogen bonds, etc.<sup>58–60</sup> The lattice energy is then calculated as a sum of pair interaction energies per asymmetric unit.

The additive scheme based on eq 2 provides crystal lattice energies that are close to the experimental sublimation enthalpies for single- and multiple-component molecular crystals, as shown in refs 61–63.

In an alternative scheme, the lattice energy,  $E_{\text{latt}}$ , of an *n*-component crystal is derived from the DFT-D3 computations as a difference of the total ZPVE-corrected energies of a relaxed crystal,  $E^{\text{cryst}}$ , and isolated molecules,  $E^{\text{mol}}$ :

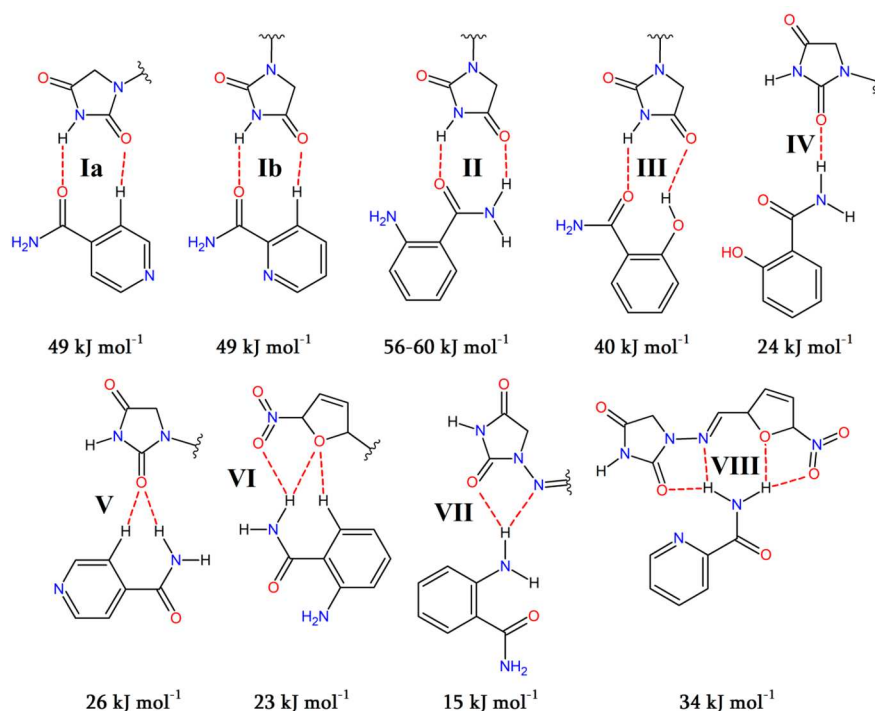
$$E_{\text{latt}} = \sum_{i=1}^n E_i^{\text{mol}} - \frac{E^{\text{cryst}}}{Z} \quad (3)$$

The counterpoise correction of the basis set superposition error was realized using the MOLEBSSE procedure.<sup>64</sup> The technical details and limitations of this approach have been described in greater detail in our previous work.<sup>65</sup>

**2.13.3. Molecular Electrostatic Potential (MEP) Calculations.** The molecular electrostatic potential surfaces (MEPs)<sup>66</sup> of the NFT and selected cofomers were generated at the B3LYP/aug-cc-pVTZ level of theory using Gaussian09.<sup>67</sup> All of the calculations were performed using structures with optimized geometries. The local maxima and minima sites on the molecular electrostatic potential surfaces were extracted using Multiwfn software.<sup>68</sup>

### 3. RESULTS AND DISCUSSION

**3.1. Crystal Structure Analysis and Intermolecular Interaction Energies.** The NFT molecule contains one hydrogen bond donor (the imide group) and six potential acceptors of different strengths. Such an imbalance limits the H-bonding ability in pure NFT to a single N–H···O bond with C–H···O/N bonds fulfilling the remaining acceptors and makes it easier to select cofomers with multiple donor sites to form a stable cocrystal.<sup>69,70</sup> With the aim of determining the most active hydrogen bonding sites and rationalizing the hydrogen-bonding pattern in the studied NFT cocrystals, we performed a molecular electrostatic potential (MEP) surface analysis for a relaxed isolated molecule extracted from the crystal of the parent NFT β form. The lowest MEP energy value ( $-38.9$  kcal mol<sup>-1</sup>) was found at the acceptor site corresponding to the O1 atom (the atom numbering corresponds to Figure 1), while the O2 atom of

Scheme 1. Heterosynthons Based on the N/O–H···O/N Hydrogen Bonds in the Studied Cocrystals<sup>a</sup>

<sup>a</sup>The synthon energies have been estimated as sums of the interaction energies using the QTAIMC approach.

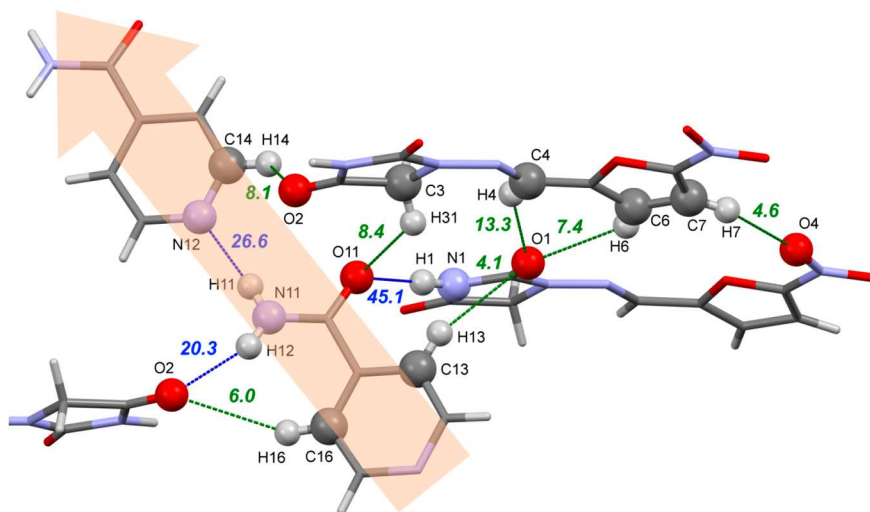


**Figure 2.** Fragment of molecular packing in the [NFT-iNA] (1:1) crystal, displaying conventional H-bonds (blue dotted lines) and C–H···O contacts (green dotted lines). The values indicate the energy in  $\text{kJ mol}^{-1}$  of a particular noncovalent interaction estimated according to the QTAIMC scheme.

the same functional group was the weakest of all the oxygen acceptor sites ( $-25.0 \text{ kcal mol}^{-1}$ ). Three oxygens in the nitrofurantoin fragment (O3–O5) had almost identical energies ( $-32.8$  to  $-32.1 \text{ kcal mol}^{-1}$ ) and thus competed for suitable donors (Figure S1). The presence of multiple donor and acceptor sites with close MEP values in NFT and cofomer molecules resulted in a complex H-bond topology. A total of nine unique heterosynthons featuring N/O–H···O/N hydrogen bonds were identified in the four NFT cocrystals studied, each of them being specific to a particular cocrystal. Scheme 1 displays the schematic representations of the synthons along with their interaction energies determined using QTAIMC. The relevant crystallographic data for the cocrystals are presented in Table S1.

**3.1.1. NFT Cocrystals with Isonicotinamide and Picolinamide.** The [NFT-iNA] (1:1) form crystallizes in the triclinic space group  $P\bar{1}$ . The asymmetric unit contains one molecule of nitrofurantoin and one molecule of isonicotinamide, held together by a moderate N1–H1···O11 bond between the strongest donor in the NFT molecule and one of the strongest acceptors in the iNA molecule (Figure 2). The resulting synthon (denoted as synthon Ia in Scheme 1) is additionally coordinated by the weak C13–H13···O1 contact, which makes the total energy equal to  $49 \text{ kJ mol}^{-1}$ . According to the MEP calculations, the amide O atom and the pyridyl N atom in the isonicotinamide molecule are closely comparable in terms of energy values ( $-36.7$  and  $-32.5 \text{ kcal mol}^{-1}$ , respectively (Figure S1); the

results are similar to those reported recently by Alvarez-Lorenzo et al.<sup>71</sup>), indicating that competition between these two acceptor sites is likely to occur in the crystalline environment. The CSD survey performed in this work (CSD version 5.43) has revealed that there are only two examples of a structural arrangement that includes cyclic imidiedione, amide, and pyridyl fragments together (Table S2): namely, cocrystals of the drug tegafur with nicotinamide and isonicotinamide.<sup>31</sup> In both cases, an imide–pyridyl heterosynthon is formed between tegafur and the cofomers. The [NFT–iNA] (1:1) crystal, however, contains hydrogen-bonded chains of iNA molecules mediated by the N11–H11···N12 H-bonds that form the amide–pyridyl homosynthon (Figure 2). A similar motif is also seen in polymorphs II–V of the parent iNA<sup>72,73</sup> as well as in the iNA cocrystals with compounds containing weak H-bond-donor groups<sup>74–76</sup> (KAXZOT, UMUYOR, VACCEK). In turn, adjacent NFT molecules interact with each other via multiple C–H···O contacts (presented in Figure 2), forming ribbons along the *a* axis. The total energy of all the C–H···O bonds within this motif equals 25 kJ mol<sup>-1</sup>. The crystal consists of alternating layers of iNA and NFT molecules held together by hydrogen bonds and stacking interactions that are oriented at an angle of 86° to each other (Figure S2).

The [NFT–PicAm] (1:1) cocrystal (*P*<sub>2</sub><sub>1</sub>/*c* space group, *Z'* = 2) shares some of the structural features with [NFT–iNA] (1:1). The strongest interaction in this crystal is the N1–H1···O11 hydrogen bond (40 kJ mol<sup>-1</sup>) formed by the strongest donor in the NFT molecule and the only strong acceptor of PicAm. Together with the C13–H12···O2 bond, it builds the amide–aromatic ketone synthon (synthon **Ib** in Scheme 1), which is topologically identical with the synthon in [NFT–iNA] (1:1) (Figure 3). The planes of the interacting molecules in [NFT–

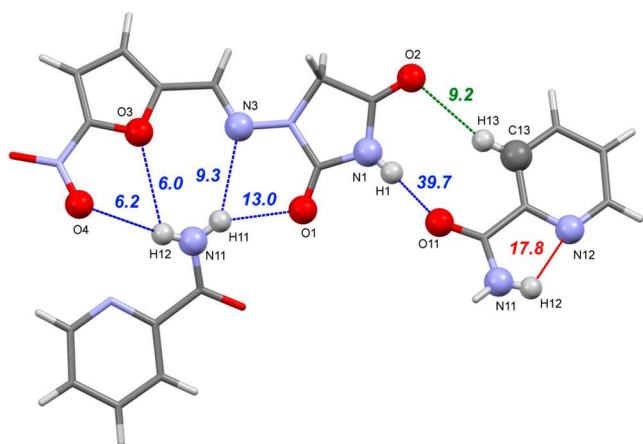


**Figure 3.** Fragment of molecular packing in the [NFT–PicAm] (1:1) crystal, displaying the conventional intramolecular H-bonds (blue dotted lines), C–H···O contacts (green dotted lines), and intramolecular H-bond (red dotted line). The values indicate the energy in kJ·mol<sup>-1</sup> of a particular noncovalent interaction estimated according to the QTAIMC scheme. The intramolecular bond in the PicAm molecule does not contribute to the lattice energy.

iNA] (1:1) are almost perpendicular to each other; in the [NFT–PicAm] (1:1) crystal, they are located in the same plane, facilitating the layered packing. Even though the oxygen atoms of the imidazolidinedione fragment of NFT differ significantly in the MEP energy, synthons **Ia** and **Ib** have been found to be isoenergetic due to a compensation effect. In comparison to

isonicotinamide, the MEP value at the pyridyl N atom in picolinamide is significantly smaller (–12.9 kcal mol<sup>-1</sup>) due to the influence of the amide group and does not seem to be a competitive counterpart to the amide group carbonyl oxygen (Figure S1). As a result, there is no evidence of hydrogen bonding between the picolinamide molecules in the [NFT–PicAm] (1:1) cocrystals. Instead, the amide group of the PicAm molecule forms two bifurcated hydrogen bonds with the NFT acceptor atoms with a total energy of 34 kJ mol<sup>-1</sup> (synthon **VIII**). An identical four-centered coordination is observed in the crystal structure of the remarkably stable NFT monohydrate. However, the cofomer molecules are not coplanar with each other, which leads to steric hindrance. To accommodate both molecules, NFT adopts a bent conformation, which facilitates the formation of hydrogen-bonded NFT and PicAm spirals. The overlapping spirals are held together by the C–H···O/N contacts and other interactions, building the crystal lattice (Figure S3).

**3.1.2. NFT Cocrystals with 2-Hydroxybenzamide and 2-Aminobenzamide.** The asymmetric unit of [NFT–2OHBZA] (1:1) contains one NFT molecule and one 2OHBZA molecule. The hydroxyl O atom in the 2OHBZA molecule acts as a second acceptor, with the MEP energy being close to that of the amide oxygen (–29.6 kcal mol<sup>-1</sup> vs –31.2 kcal mol<sup>-1</sup>), leading to competition between the two bonding sites (Figure S1). The best donor in the NFT molecule is paired with one of the strong acceptors of 2OHBZA, forming the strongest N1–H1···O11 bond with  $E_{\text{int}} = 33.2$  kJ mol<sup>-1</sup>, in accordance with Etter’s rule<sup>77,78</sup> (Figure 4). However, a QTAIMC analysis revealed a (3;–1) critical point between the hydroxyl H12 atom and the carbonyl O2 atom of the NFT molecule, which implies the existence of a weak O12–H12···O2 H-bond (Figure 4). Together with the N1–H1···O11 bond, it builds a unique cyclic heterosynthon with *R*<sub>2</sub><sup>2</sup>(10) topology (synthon **III** in Scheme 1). The second-best N–H donor in the 2OHBZA molecule is bound to the strongest NFT acceptor to form a nonbifurcated N11–H10···O1 bond with  $E_{\text{int}} = 23.6$  kJ mol<sup>-1</sup> (synthon **IV**). The combination of these two H-bonding motifs results in the tetrameric units presented in Figure 4, which are further assembled into 2D layers via C–H···O/N contacts. The parallel layers are held together by  $\pi$ -stacking interactions in a way resembling the crystal packing in the  $\beta$ -form of pure NFT (Figure S4). According to a QTAIMC analysis, the strongest donor in the 2OHBZA molecule (N11–H11 group) and two acceptor atoms of NFT (O3 and N3) are not involved in any intermolecular hydrogen bonds, which violates Etter’s rules and possibly indicates a low stability of this structure. In all of the 2OHBZA cocrystals observed in the CSD, the “side” N–H···X hydrogen bond formed by the H11 atom would always point to the acceptor that is located outside the molecular plane. The layered packing of the molecules in [NFT–2OHBZA] (1:1) presented in Figure S4 (similar to that in the pure NFT crystal) hinders the H-bonding between the fragments that belong to different layers; hence, the N–H group and carbonyl acceptor sites become inaccessible for hydrogen bonding. The QTAIMC analysis has also detected a destabilizing intramolecular H···H contact between the amide H11 hydrogen and phenyl C17–H17 group at the ortho position of 2OHBZA, which causes the molecule to deviate from planarity.

In comparison to 2OHBZA, the 2AmBZA molecule has an additional strong H-bond donor, which is potentially able to bind the excess NFT acceptor sites. The asymmetric unit of the [NFT–2AmBZA] (1:1) crystal (*P*<sub>1</sub> symmetry) contains two

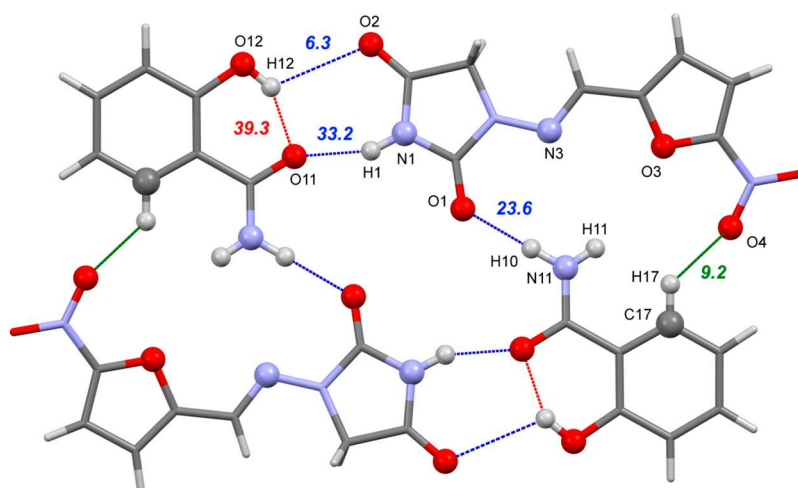


**Figure 4.** Hydrogen-bonded tetrameric units in the [NFT-2OHBZA] (1:1) crystal showing the conventional intramolecular H-bonds (blue dotted lines), C–H···O contacts (green dotted lines), and intramolecular H-bonds (red dotted lines). The values indicate the energy in  $\text{kJ}\cdot\text{mol}^{-1}$  of a particular noncovalent interaction estimated according to the QTAIMC scheme. The intramolecular bond in the 2OHBZA molecule does not contribute to the lattice energy.

independent pairs of NFT and 2AmbZA molecules. The NFT conformation in this cocrystal is different from that of the other three structures considered in this work, as the nitrofur moiety is rotated by  $180^\circ$  around the C–C bond with respect to the rest of the molecule. An analysis from the CSD of 78 crystal structures containing nitrofurantoin has revealed that only 15% of NFT molecules have the “twisted” conformation observed in [NFT-2AmbZA] (1:1). No clear connection between the chemical nature of the coformer and the resulting NFT conformation has been established, however. The differences in the MEP distribution between the “original” and “twisted” conformations mostly affect the relative strength of acceptor sites, but the difference is comparable to the method error (Figure S1).

Although all of the obtained crystal structures have both amide and imide groups, a cyclic imide–amide synthon (synthon II) formed by two N–H···O hydrogen bonds is observed only in [NFT-2AmbZA] (1:1). The energy of these synthons in two symmetry-inequivalent NFT-2AmbZA dimers equals 60 and  $56 \text{ kJ mol}^{-1}$ , respectively (Figure 5). The bifurcated side N–H···O hydrogen bonds (synthon VI) formed by the strongest donor in 2AmbZA (Figure S1) unite the dimers into spiral chains, which are further stabilized in the crystal through C–H···X bonds and other noncovalent interactions (Figure 5). The herringbone packing of the molecules makes all potential donor and acceptor groups accessible to intermolecular interactions (Figure S5), resulting in a higher fraction of H-bonds and a higher lattice energy of this crystal (see Section S2 in the Supporting Information).

In summary, the  $-\text{N}_{\text{im}}-\text{H}\cdots\text{O}=\text{C}-\text{N}_{\text{amide}}\text{H}_2$  hydrogen bond between the NFT and coformers appears to be the strongest intermolecular interaction and the only interaction that persists in all of the studied cocrystals. This fact agrees well with the CSD statistics, which show that, if the cyclic imide and amide groups coexist in a crystal structure, there is a 75.4% probability that at least one  $-\text{N}_{\text{im}}-\text{H}\cdots\text{O}=\text{C}-\text{N}_{\text{amide}}\text{H}_2$  hydrogen bond would be formed, while a closed-ring imide–amide heterosynthon is expected in 54.7% of the cases (Table S2). Despite the structural similarity of the coformers, the obtained crystals contain no isostructural packing motifs. The diversity of the observed heterosynthons agrees well with the presence of multiple

hydrogen-bonding sites with close energy values computed from the MEP surface data. The energy of a particular heterosynthon appears to depend more on the nature of the H-bond donor rather than that of the acceptor, which is similar to the conclusion made in the theoretical work studying a range of isoniazid cocrystals with carboxylic acids.<sup>79</sup> In addition, the bifurcation of a bond does not lead to a visible interaction energy increase. Assuming that the cocrystal formation from the initial components is mostly governed by hydrogen bonding, we can order the considered crystals by the heterosynthon energy from the least to the most favorable: [NFT-2OHBZA] (1:1) (III + IV) < [NFT-iNA] (1:1) (I + V) < [NFT-PicAm] (1:1) (I + VIII) < [NFT-2AmbZA] (1:1) (II + VI + VII).

**3.2. Thermodynamics of Cocrystal Formation.** A number of experimental methods to determine the thermodynamic parameters of cocrystal formation have been reported in the literature. The key characteristic responsible for the relative stability of a cocrystal in relation to its constituents is the free-energy change,  $\Delta_{\text{form}}G^\circ$ , of the cocrystallization reaction. The Gibbs energy of cocrystal formation at a particular temperature can be experimentally obtained using the solubility values of a cocrystal and its components in the same solvent by the relationship<sup>18,20,80–82</sup>

$$\Delta_{\text{form}}G^\circ = -RT \ln \left( \frac{a_A^x \cdot a_B^y}{K_{\text{sp}}} \right) \quad (4)$$

where  $a_A$  and  $a_B$  represent the activities of pure compounds A and B in a saturated solution, which are usually approximated by the corresponding molar concentration,  $K_{\text{sp}}$  is the solubility product of a [A–B] cocrystal ( $x:y$ ),  $T$  is the temperature, and  $x$  and  $y$  are the stoichiometric coefficients.

An accurate evaluation of the solubility product values in a solvent of interest requires the construction of a phase solubility diagram, which not only makes it possible to establish the cocrystal stability region but also provides information about the associated equilibria in the solution, such as complexation between the components.<sup>83–85</sup> In this work, the solubilities of the NFT cocrystals as a function of coformer concentration were determined in acetonitrile at  $25.0^\circ\text{C}$ , and the values of the

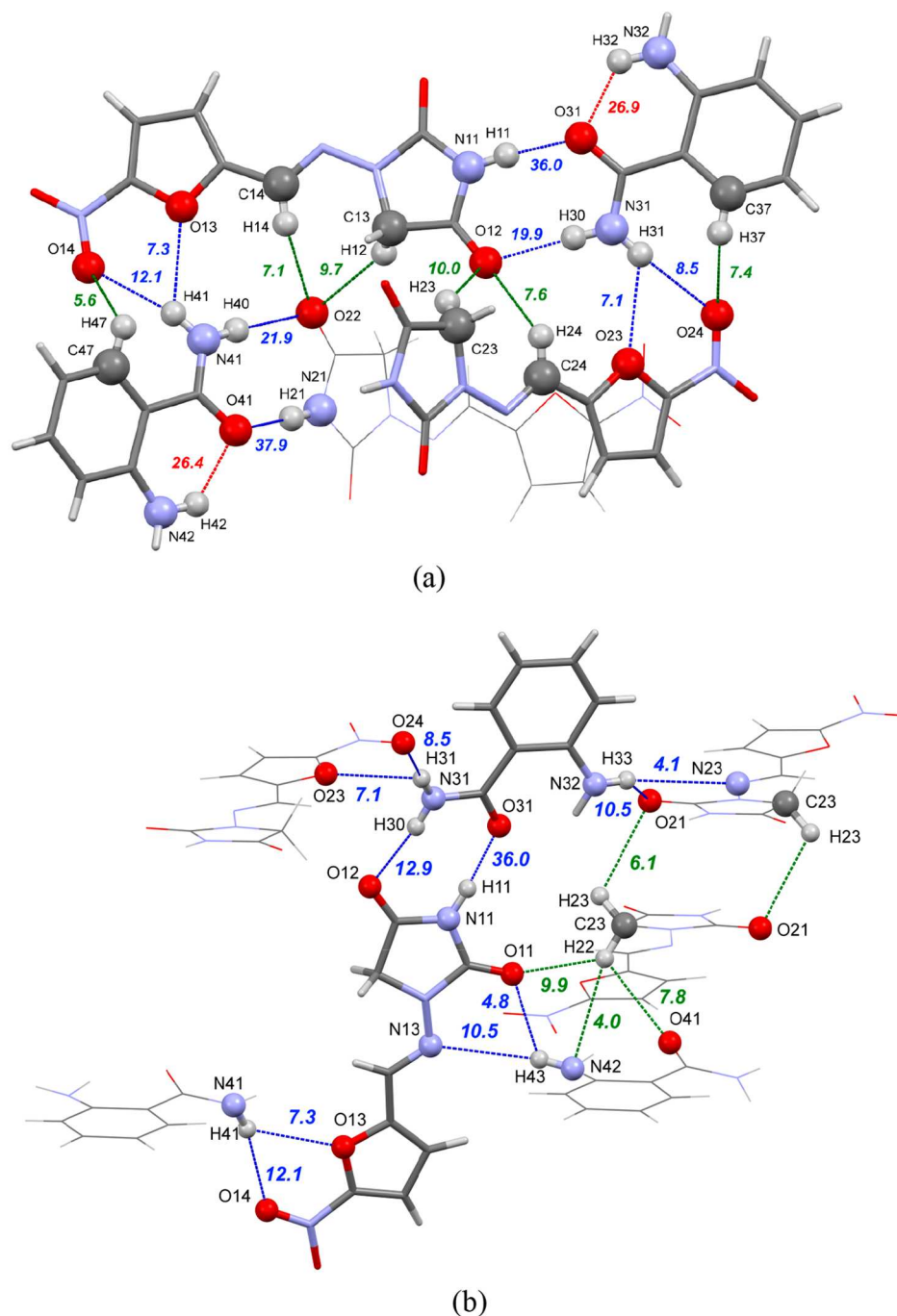


**Figure 5.** (a) Part of the hydrogen-bond network in the [NFT-2AmBZA] (1:1) crystal showing the conventional intermolecular H-bonds (blue dotted lines), C-H...O contacts (green dotted lines), and intramolecular O-H...O bonds (red dotted lines). The values indicate the energy in kJ mol<sup>-1</sup> of a particular noncovalent interaction estimated according to the QTAIMC scheme. (b) Conventional intermolecular H-bonds (blue dotted lines) and C-H...O contacts (green dotted lines) binding the single heterodimer in [NFT-2AmBZA] (1:1) to the crystalline environment. The values indicate the energy in kJ mol<sup>-1</sup> of a particular noncovalent interaction estimated according to the QTAIMC scheme.

solubility product ( $K_{sp}$ ) and complexation constants ( $K_{11}$ ) were derived from the equation (assuming that  $K_{11} \cdot K_{sp} \ll [B]_T^{83}$ )

$$[A]_T = \frac{K_{sp}}{[B]_T} + K_{11} \cdot K_{sp} \quad (5)$$

where  $[A]_T$  and  $[B]_T$  are the total analytical concentrations of the components in equilibrium with the cocrystal and  $K_{11}$  is the 1:1 complexation constant.

The experimental phase solubility diagrams for the [NFT-iNA] (1:1), [NFT-PicAm] (1:1), and [NFT-2AmBZA] (1:1) cocrystals are shown in Figure S6. The thermodynamic constants ( $K_{sp}$  and  $K_{11}$ ) derived by a nonlinear fit of eq 5 to the experimental concentrations of the components are provided in Table S6. The [NFT-iNA] (1:1) solid form was found to be the only congruently saturating cocrystal in acetonitrile. In contrast, the [NFT-2OHBZA] (1:1), [NFT-PicAm] (1:1), and [NFT-2AmBZA] (1:1) cocrystals dissolved

incongruently in the chosen solvent, indicating that they were more soluble than the parent drug. In fact, for [NFT-2OHBZA] (1:1), the cocrystal stability region was found to be significantly shifted toward the region of high coformer concentrations ( $[2\text{OHBZA}]_{\text{T}} > 0.4 \text{ M}$ ) and appeared to be too narrow for a reliable determination of the phase solubility diagram. In this case, the  $K_{11}$  complexation constant was evaluated in a separate experiment (Figure S7) by the equation

$$[A]_{\text{T}} = [A]_0 + \left( \frac{K_{11} \cdot [A]_0}{1 + K_{11} \cdot [A]_0} \right) \cdot [B]_{\text{T}} \quad (6)$$

where  $[A]_0$  is the intrinsic solubility of A in a solvent.

Then, the solubility product value ( $K_{\text{sp}}$ ) for [NFT-2OHBZA] (1:1) was calculated by eq 5, using the  $K_{11}$  parameter and the total concentrations of the components at the eutectic point,<sup>5,84,86,87</sup> where both the cocrystal and drug coexist in equilibrium with the solution. The  $K_{\text{sp}}$  parameter for the cocrystals and the experimental solubilities for their corresponding pure components in acetonitrile are given in Table S6, while the estimated Gibbs energies of cocrystallization are provided in Table 1. Although the resulting  $\Delta_{\text{form}}G^\circ$  values for all of the

**Table 1. Thermodynamic Functions (in  $\text{kJ mol}^{-1}$ ) of the NFT Cocrystal Formation at 25.0 °C**

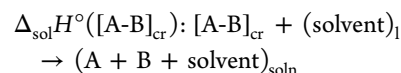
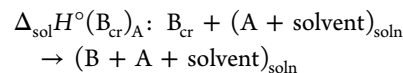
cocrystal	$\Delta_{\text{form}}G^\circ$	$\Delta_{\text{form}}H^\circ$	$T\Delta_{\text{form}}S^\circ$
[NFT-iNA] (1:1)	$-4.7 \pm 0.4$	$1.3 \pm 0.6$	$6.0 \pm 0.7$
[NFT-PicAm] (1:1)	$-4.9 \pm 0.5$	$-4.4 \pm 0.7$	$0.6 \pm 0.8$
[NFT-2AmbZA] (1:1)	$-4.5 \pm 0.5$	$-3.3 \pm 0.8$	$1.3 \pm 1.1$
[NFT-2OHBZA] (1:1)	$-0.6 \pm 0.4$	$-0.3 \pm 0.6$	$0.3 \pm 0.7$

systems were negative, suggesting that the cocrystal formation from the individual components was spontaneous,<sup>55</sup> the driving force of [NFT-2OHBZA] (1:1) formation was found to be remarkably lower than that of the other NFT cocrystals. This fact indicates that the single-phase packing arrangement of [NFT-2OHBZA] (1:1) is only slightly more thermodynamically stable than that of the physical mixture of NFT and 2OHBZA and explains the difficulty in the preparation of this binary crystalline form.

It is well-known that the formation Gibbs energy is a complex parameter, resulting from the competition between the enthalpy and entropy terms, with each of them in turn depending on the relative strength of the intermolecular forces and order in both the multicomponent system and the parent components. Two approaches to determining cocrystallization enthalpy have been developed. The first is a solvent-free method that solely relies on differential scanning calorimetry measurements of the integral enthalpy changes on melting the cocrystals and the physical mixture of the component crystals.<sup>23,25,88–90</sup> This technique, however, is not applicable to thermally unstable systems, such as NFT cocrystals that, according to TG results, undergo rapid thermal decomposition above the corresponding melting point (Figure S8). Hence, an alternative procedure that utilizes solution calorimetry measurements was applied in this work.<sup>91–95</sup> In this method, the standard enthalpy of the cocrystal formation reaction can be calculated using the relationship (assuming 1:1 stoichiometry)

$$\Delta_{\text{form}}H^\circ = \Delta_{\text{sol}}H^\circ(A_{\text{cr}}) + \Delta_{\text{sol}}H^\circ(B_{\text{cr}})_A - \Delta_{\text{sol}}H^\circ([A-B]_{\text{cr}}) \quad (7)$$

where  $\Delta_{\text{sol}}H^\circ(A_{\text{cr}})$ ,  $\Delta_{\text{sol}}H^\circ(B_{\text{cr}})_A$ , and  $\Delta_{\text{sol}}H^\circ([A-B]_{\text{cr}})$  represent the standard molar enthalpies of the following processes, at 298.15 K, determined by solution calorimetry:



The obtained experimental enthalpies of the solution are summarized in Table S7, while the corresponding enthalpies of cocrystallization calculated from eq 7 are provided in Table 1.

According to the results of the calorimetric measurements, the process of [NFT-iNA] (1:1) formation is endothermic. On consideration of the negative  $\Delta_{\text{form}}G^\circ$  value, the cocrystallization reaction between NFT and iNA is entropically favored and dominated by the  $T\Delta_{\text{form}}S^\circ$  term. Even though examples of entropically driven cocrystallization reactions are relatively rare, since only a handful of cases have been observed experimentally,<sup>23–25</sup> a recent theoretical study by Perlovich estimated that the fraction of such systems is about 30%.<sup>26</sup> In the case of [NFT-2OHBZA] (1:1), the obtained  $\Delta_{\text{form}}H^\circ$  value is not statistically different from zero (Table 1), which shows that the low driving force of the cocrystallization process of this solid form is mainly due to the lack of energy (enthalpy) gain most often associated with cocrystal formation.<sup>22</sup> A further analysis of the experimental data revealed that the thermodynamic stability of the [NFT-PicAm] (1:1) and [NFT-2AmbZA] (1:1) cocrystals is primarily of enthalpic nature, since the formation process is exothermic in both cases (Table 1). The fact that the absolute values of the Gibbs energies for these two cocrystals are slightly higher than those of the formation enthalpies, i.e.  $|\Delta_{\text{form}}G^\circ| > |\Delta_{\text{form}}H^\circ|$ , is likely to be result of the utilization of analytical concentrations of the components in saturated solutions instead of their thermodynamic activities as eq 4 requires. Although the  $\Delta_{\text{form}}G^\circ$  values can be further refined by evaluating the activity coefficients of species in the liquid phase at the equilibrium state to account for nonideal behavior,<sup>96,97</sup> this aspect is beyond the scope of the current work. Overall, the NFT cocrystals with the structurally related coformers reported here demonstrate a wide spectrum of thermodynamic formation properties that are challenging to deduce based on structural data alone. The theoretically estimated cocrystallization energies obtained from the DFT-D3 and QTAIME lattice energy calculations agree only semiquantitatively with the experimental  $\Delta_{\text{form}}H^\circ$  values. Even though the predicted formation energies for the three cocrystals considered follow the experimental trend, with the [NFT-2OHBZA] cocrystallization energy being close to zero and those of [NFT-2AmbZA] (1:1) and [NFT-PicAm] (1:1) being the most stable in terms of energy (Table S5), both computational methods failed to predict the endothermic nature of the cocrystallization reaction between NFT and iNA. Some plausible reasons for this discrepancy are discussed in Section S2 of the Supporting Information.

**3.3. Solubility and Solution Stability of the Nitrofurantoin Cocrystals.** The intrinsic thermodynamic solubility of a cocrystal is determined by its solubility product or  $K_{\text{sp}}$ , which represents the product of the equilibrium molar concentrations (or activities) of the cocrystal constituents in the same molecular state as in the cocrystal.<sup>87</sup> The value of this

**Table 2.** Experimental Solubility ( $S_{cc}$ ) of the NFT Cocrystals, Solubility Advantage (SA), Eutectic Constants ( $K_{eu}$ ) and  $K_{sp}$  Values at the Equilibrium pH and 37.0 °C

	equilibrium pH	$S_{cc}$ , M <sup>a</sup>	$K_{eu}$ <sup>b</sup>	SA <sup>c</sup>	$pK_{sp}$ <sup>d</sup>
		Initial pH 1.2			
[NFT-iNA](1:1)	4.1	$(2.9 \pm 0.4) \times 10^{-2}$	$235 \pm 64$	$15.3 \pm 2.0$	3.2
[NFT-PicAm] (1:1)	2.3	$(1.6 \pm 0.1) \times 10^{-2}$	$106 \pm 14$	$10.3 \pm 0.7$	3.8
[NFT-2AmBZA] (1:1)	2.7	$(1.05 \pm 0.08) \times 10^{-2}$	$59 \pm 9$	$7.7 \pm 0.6$	4.3
[NFT-2OHBZA] (1:1)	1.3	$(5.1 \pm 0.3) \times 10^{-3}$	$16 \pm 2$	$4.0 \pm 0.2$	4.6
		Initial pH 7.4			
[NFT-iNA] (1:1)	7.3	$(4.1 \pm 0.4) \times 10^{-2}$	$101 \pm 19$	$10.0 \pm 1.0$	
[NFT-PicAm] (1:1)	7.3	$(1.8 \pm 0.1) \times 10^{-2}$	$37 \pm 4$	$6.0 \pm 0.3$	
[NFT-2AmBZA] (1:1)	7.2	$(1.0 \pm 0.1) \times 10^{-2}$	$15 \pm 1$	$3.8 \pm 0.1$	
[NFT-2OHBZA] (1:1)	7.2	$(7.2 \pm 0.2) \times 10^{-3}$	$9 \pm 1$	$3.0 \pm 0.1$	

<sup>a</sup>Calculated according to eq 8. <sup>b</sup> $K_{eu} = [\text{coformer}]_{eu}/[\text{NFT}]_{eu}$ .<sup>111</sup> <sup>c</sup>Calculated according to eq 9 <sup>d</sup> $pK_{sp} = -\log K_{sp}$ .

parameter in a particular solvent depends only on the temperature and serves as an indicator of the relative strength of the drug and coformer intermolecular interactions in the cocrystal with respect to that in the solvent.<sup>98</sup> In contrast, the effective cocrystal solubility calculated on the basis of the total analytical concentrations of the components in a solution can significantly vary with the pH of the dissolution medium and change in the presence of solubilization agents or solution complexation.<sup>5,99,100</sup> The apparent or kinetic cocrystal solubility is associated with the transient API concentration in the supersaturated solution generated during the dissolution of incongruently soluble cocrystals and is usually interpreted within the framework of the “spring and parachute” model.<sup>3,101</sup> The apparent cocrystal solubility is known to be both condition and compound specific, as its value depends on the cocrystal solubility advantage, supersaturation level, cocrystal dissolution rate and drug crystallization tendency, and presence of nucleation and crystallization inhibitors.<sup>102–110</sup> Thus, ranking the dissolution performance of cocrystals on the basis of their kinetic parameters, such as the maximum drug concentration or area under the curve, can be misleading unless the thermodynamic solubility values are determined.<sup>5,87</sup>

The vast majority of pharmaceutical cocrystals dissolve incongruently in an aqueous medium since they have higher solubility in comparison to the drug parent form. Therefore, there is a driving force toward a phase transition into a more thermodynamically stable solid form of a compound in the aqueous medium. The NFT cocrystals reported here are no exception and undergo a solvent-mediated transformation upon dissolution in aqueous buffer solutions to form the monohydrate of the drug (form II), as the preliminary slurry experiments evidenced. It should be noted that low stability, resulting in incongruent solubility in water, has been also observed for NFT cocrystals with urea,<sup>41</sup> L-arginine,<sup>34</sup> 4-hydroxybenzoic and citric acids, nicotinamide, and L-proline.<sup>43</sup> In order to evaluate the effective thermodynamic solubility of the NFT cocrystals under physiologically relevant conditions, the approach developed by Rodríguez-Hornedo’s group was applied.<sup>98</sup> In this method, the equilibrium solubility of a cocrystal is determined at the eutectic point, which represents a doubly saturated solution with respect to the drug and cocrystal and is the eutectic point for these two solids and the solution at given pH and temperature values.<sup>5,111,112</sup> Since the eutectic point is independent of the mass of each phase at equilibrium and can be achieved regardless of the solubility relationship between the cocrystal and drug, this method provides a reliable way to evaluate the thermodynamic

solubility of highly soluble cocrystals, inaccessible otherwise.<sup>113,114</sup>

In the general form, the cocrystal solubility is related to the eutectic concentration of the components by the equation<sup>87</sup>

$$S_{cc} = \left( \frac{[\text{drug}]_{eu}^a [\text{coformer}]_{eu}^b}{a^a b^b} \right)^{1/a+b} \quad (8)$$

where  $[\text{drug}]_{eu}$  and  $[\text{coformer}]_{eu}$  are the eutectic concentrations of the components and  $a$  and  $b$  are the stoichiometric coefficients of the drug and the coformer, respectively. A reliable procedure of the solubility measurement using this approach requires information about not only the equilibrium concentration of the cocrystal constituents and the final value of the solution pH but also the composition of the solid phase at equilibrium. In this work, all three of the mentioned parameters have been carefully monitored.

The solubility values of the NFT cocrystals at two different pHs and 37.0 °C (Table 2) were calculated using eq 8 and the experimental eutectic concentrations of NFT and the cofomers (Table S8). According to Rodríguez-Hornedo, the ratio of the solution concentrations of the cocrystal components at the eutectic point, also known as the cocrystal eutectic constant or  $K_{eu}$ , is one of the key parameters that determine the cocrystal thermodynamic stability relative to the drug under given conditions.<sup>5</sup> A 1:1 cocrystal is considered to be thermodynamically stable if its  $K_{eu}$  value does not exceed 1; otherwise, the cocrystal is less thermodynamically stable and more soluble than the parent drug. The experimental data clearly indicate that all of the considered NFT cocrystals tend to be more soluble than the NFT monohydrate in the aqueous medium, as the resulting values of the  $K_{eu}$  parameter range between 9 and 235 (Table 2). It has also been proven that the cocrystal eutectic constants can be utilized to evaluate the cocrystal solubility advantage over the drug (SA) in a particular solvent using the following relationship (assuming no or minor complexation between the components in the solution):<sup>87</sup>

$$K_{eu} = \frac{b}{a} SA^{a+b/b} \quad (9)$$

As Table 2 shows, NFT cocrystallization with the selected aromatic amides can potentially increase the drug solubility from 3 to 15 times, depending on the pH and coformer used. It is evident that the highest solubility can be achieved by taking advantage of the most water soluble coformer: i.e., isonicotinamide.

An evaluation of the solubility–pH behavior of the NFT cocrystals over the entire range of the physiologically relevant pH values requires knowing the  $K_{sp}$  parameter for each multicomponent phase. The general equation that relates intrinsic ( $K_{sp}$ ) and effective ( $S_{cc}$ ) solubilities of a cocrystal can be written in the form<sup>86</sup>

$$S_{cc} = \left( \frac{K_{sp}}{a^a b^b} \delta_{drug}^a \delta_{coformer}^b \right)^{1/a+b} \quad (10)$$

where  $K_{sp}$  is the cocrystal solubility product and  $\delta_{drug}$  and  $\delta_{coformer}$  are the ionization terms for the drug and the coformer, respectively. The  $K_{sp}$  values of the NFT cocrystals (Table 2) were calculated using the experimental solubility measured at equilibrium pHs and the following ionization constants of the components taken from the literature or calculated in ChemAxon:  $pK_a(\text{NFT}) = 7.2$ ,  $pK_a(\text{iNA}) = 3.7$ ,  $pK_a(\text{PicAm}) = 1.9$ ,  $pK_a(\text{2OHBZA}) = 8.1$ , and  $pK_a(\text{2AmBZA}) = 2.8$ .

Figure 6 shows that the obtained cocrystals are more soluble than the parent drug over the entire pH range, as no intersection

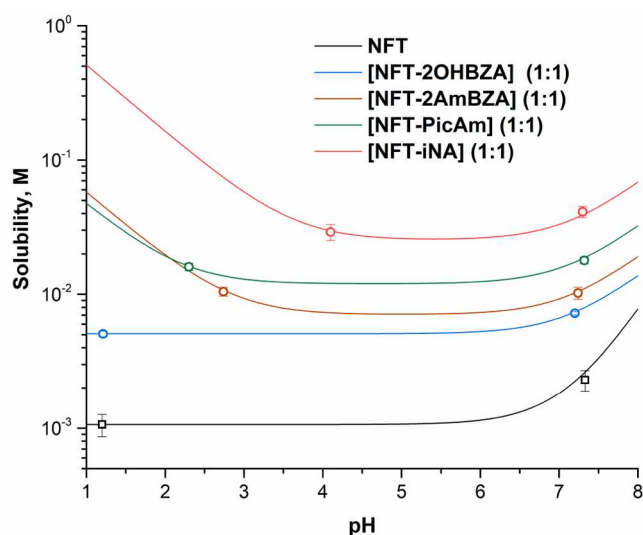


**Figure 6.** Solubility–pH dependence of NFT and its cocrystals calculated on the basis of eq 10. The experimental cocrystal solubilities at different pHs and 37.0 °C are represented by empty colored circles. The empty black squares show the experimental NFT solubility.

points between the solubility curves are observed. In addition, cocrystallization alters the NFT solubility–pH dependence. Although the solubility of the original NFT is slightly pH dependent and remains virtually constant up to pH 6.0, the solubility of the NFT cocrystals with weak bases, such as iNA, PicAm, and 2AmBZA, increases under acidic conditions due to extensive ionization of the cofomers. Since 2OHBZA is nonionizable within the considered pH range, the solubility behavior of the [NFT-2OHBZA] (1:1) cocrystal is controlled by its  $K_{sp}$  value and NFT ionization degree (Figure 6).

**3.4. Dissolution Studies of the Nitrofurantoin Cocrystals.** The comprehensive analysis of the thermodynamic solubility performed in the previous section unambiguously showed that the NFT cocrystals were more soluble than the parent drug and were expected to exhibit superior dissolution performance within the physiologically relevant pH range. However, the dissolution profiles of the powder samples of the cocrystals obtained under nonsink conditions at pH 7.4 and 37.0

°C displayed no improvement in the apparent solubility of NFT in comparison to that of the initial drug (Figure 7a). After 6 h of

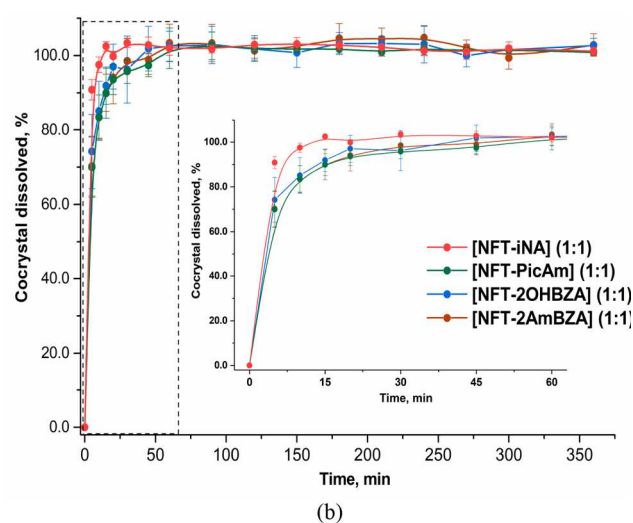
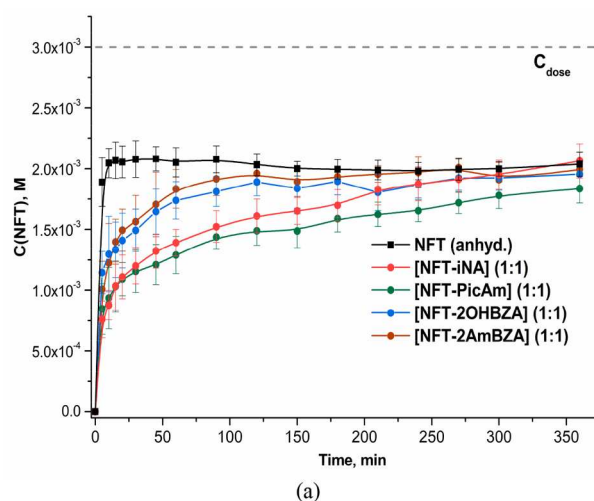


**Figure 7.** (a) Dissolution profiles of the anhydrous NFT and the cocrystals in a pH 7.4 buffer at 37.0 °C. (b) Percentage of the cocrystal dissolved. Inset: detailed illustration of the data within the 0–60 min time frame.

the experiment, the bulk phase concentration of the tested solid forms reached similar plateau concentrations, corresponding to that of the NFT monohydrate (61–69% of the theoretical NFT dose concentration,  $C_{dose}$ ). The complete transformation of all the cocrystals and anhydrous NFT into the NFT monohydrate phase was also confirmed by the PXRD analysis of the residual materials collected at the end of the experiment (Figure S9). As Figure 7a illustrates, there was no evidence of supersaturation generated during the dissolution of the cocrystals, indicating that the so-called particle surface solution-mediated phase transformation process (PS-SMPT) took place during the dissolution. In contrast to the bulk-phase SMPT, which is mainly associated with the spring and parachute mechanism of dissolution, the PS type of SMPT occurred locally at the particle surface before the drug molecules diffused into the solution bulk and the supersaturation stage of the process was not attained.<sup>103,115–118</sup> Similarly to the highly soluble carbamazepine cocrystals, the PS-SMPT dissolution behavior of which has

been studied recently,<sup>102</sup> the novel NFT solid forms also rapidly transformed to the NFT hydrate without any detectable sign of supersaturation. Figure 7b shows that nearly 100% of [NFT-iNA] (1:1) and 85–89% of [NFT-PicAm] (1:1), [NFT-2AmBZA] (1:1), and [NFT-2OHBZA] (1:1) dissolved/dissociated after only 10 min of the dissolution process, while the solution remained undersaturated in comparison to the drug content at the same time point, indicating that the dissolution rates of NFT and the coformers became decoupled almost immediately after coming in contact with the solvent and the former was supposedly controlled by the PS-SMPT process product: i.e.,  $\text{NFT}\cdot\text{H}_2\text{O}$ .

In order to study the dissolution behavior of the NFT cocrystals in a more controllable and consistent manner, we also investigated the drug and coformer release from tablets made of different solids using the rotating-basket method (USP apparatus 1) and the same experimental conditions as described previously. All of the tested samples contained an equivalent amount of NFT (by weight), either in the form of a cocrystal or in the form of anhydrous NFT. As Figure 8a shows, a statistically significant improvement in the dissolution rate and the cumulative amount of NFT released was observed only for [NFT-iNA] (1:1), while for the rest of the cocrystals, the dissolution performance was comparable to that of neat NFT.

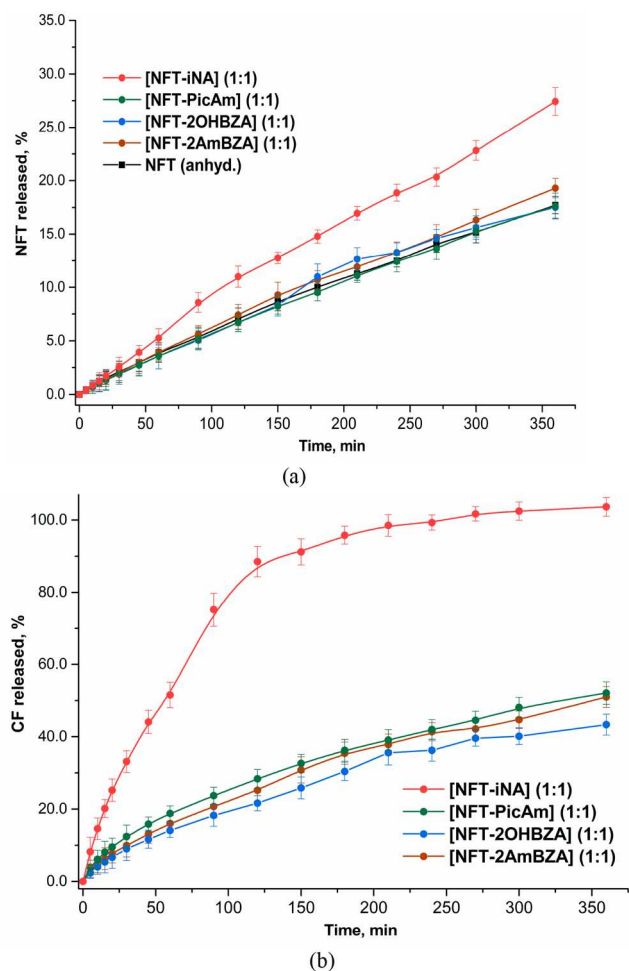


**Figure 8.** Cumulative percentages of NFT (a) and coformers (b) released during dissolution using the rotating-basket method (USP apparatus 1) at pH 7.4 and 37.0 °C.

The same conclusions can be drawn on considering the values of the difference ( $f_1$ ) and similarity ( $f_2$ ) factors, which are widely used indices for determining the degree of similarity/dissimilarity between dissolution profiles of pharmaceutical formulations.<sup>119</sup> According to the calculated  $f_1$  and  $f_2$  numerical values, the release profiles of NFT and the [NFT-PicAm] (1:1), [NFT-2AmBZA] (1:1), and [NFT-2OHBZA] (1:1) cocrystals should be considered to be similar, as  $f_1$  was found to be less than 15 and  $f_2$  was greater than 50 (Table S9). With regard to [NFT-iNA] (1:1), both parameters denoted an unambiguous difference between the dissolution profiles of the cocrystal and the drug (Table S9). A higher NFT release rate from [NFT-iNA] (1:1) is likely to be associated with a higher solubility and dissolution rate of the entire cocrystal, as is seen on the dependences of the percentage of the cocrystal dissolved as a function of time shown in Figure 8b. It can be supposed that, in the case of [NFT-iNA] (1:1), the cocrystal dissolution successfully competes with drug nucleation and precipitation processes on the exposed surface of the sample, allowing an excess amount of NFT to be released in the bulk of the solution and leading to its increased concentration.

In contrast, the [NFT-PicAm] (1:1), [NFT-2AmBZA] (1:1), and [NFT-2OHBZA] (1:1) cocrystals demonstrated virtually identical dissolution behaviors in terms of the relative release rate of both the coformer and the API (Figure 8a), although they had different thermodynamic solubilities. The absence of a conspicuous gain in the dissolution rate for these cocrystals can again be attributed to the rapid SMPT process on the surface of the tablets, which in this case clearly outcompetes cocrystal dissolution. As a result, the overall rate of the coformer release appeared to be lower than that of iNA and is likely to have been determined by diffusion through the upper layer of the poorly soluble NFT monohydrate. This assumption was confirmed by a mathematical treatment of the coformer release data using different kinetic models: namely, first-order, Higuchi, and Korsmeyer–Peppas models.<sup>119</sup> The results collected in Table S9 show that the best fit of the iNA release time was provided by the first-order model, whereas the Korsmeyer–Peppas equation was found to be more suitable for describing the PicAm, 2AmBZA, and 2OHBZA release profiles. The resulting values of the release exponent,  $n$ , appeared to be slightly higher than 0.5 (Table S9), suggesting that, although the release process of the coformers was mainly driven by diffusion, it was also accompanied by erosion/dissolution of the matrix consisting of  $\text{NFT}\cdot\text{H}_2\text{O}$ . These mechanistic interpretations agree well with the observed dissolution behavior of the cocrystals.

In summary, the preliminary characterization of the NFT cocrystals performed here indicates that, in their native form, the considered solid forms are unlikely to provide a sufficient therapeutic concentration *in vivo* due to rapid nucleation and crystallization of NFT monohydrate in aqueous media. Thus, additional formulation strategies, e.g. utilization of crystallization inhibitors, should be considered to suppress the unwanted SMPT process and to unlock the supersaturation potential of the cocrystals.<sup>102–110</sup> This issue will be addressed in our further work on NFT multicomponent solid forms.

**3.5. Influence of Cocrystallization on NFT Permeability.** In addition to solubility, an essential prerequisite for good bioavailability of orally administered drugs is sufficient membrane permeability.<sup>120</sup> Although pharmaceutical cocrystals are a prominent tool for enhancing the API solubility and dissolution rate, the presence of a coformer can affect API absorption, decreasing its membrane permeability. Therefore,

permeability control should be applied at the early stages of cocrystal design. Since unformulated NFT cocrystals undergo rapid SMPT in aqueous media and are unlikely to provide an increased flux rate of the drug, the main goal of this part of the work was to evaluate the influence of cofomers on the NFT permeation behavior.

The diffusion behavior of NFT and its cocrystals was first studied using a Franz diffusion cell with a lipophilic biomimetic membrane. The diffusion of all the solids was measured in a pH 7.4 buffer solution at different time intervals. The plots of cumulative drug diffused and flux vs the per unit time are shown in Figure 9 and Figure S10. As Figure 9 shows, the cumulative

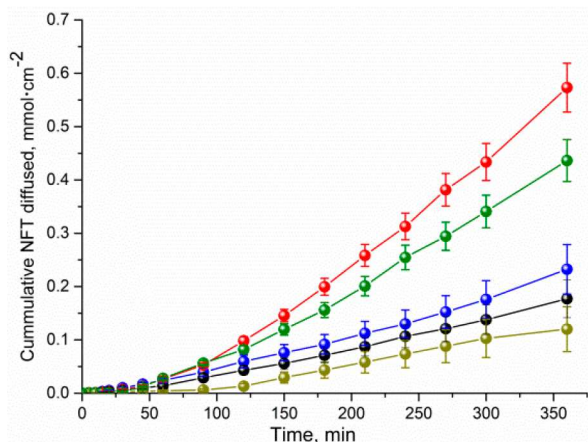


**Figure 9.** Cumulative amount of NFT and its cocrystals diffused across the membrane at different intervals. The measurements were made over a time period of 6 h in a pH 7.4 phosphate buffer (—●—, NFT·H<sub>2</sub>O; —●— (red), [NFT-iNA] (1:1); —●— (green), [NFT-PicAm] (1:1); —●— (blue), [NFT-2OHBZA] (1:1); —●— (dark yellow), [NFT-2AmBZA] (1:1)).

amount of NFT diffused increases slowly with time for all of the studied solids. The [NFT-iNA] (1:1) and [NFT-PicAm] (1:1) cocrystals exhibit the best diffusion behavior among all of the cocrystals. For [NFT-2OHBZA] (1:1) and [NFT-2AmBZA] (1:1), the cumulative amount of the drug diffused is comparable to that of the parent NFT. The [NFT-2AmBZA] cocrystal also exhibits an initial slow increase in diffusion, which reaches a steady state after 2.5 h (Figure S10). Overall, the higher flux of the [NFT-iNA] and [NFT-PicAm] cocrystals could be due to the higher solubility of iNA and PicAm in an aqueous solution in comparison to 2OHBZA and 2AmBZA.

In addition to solubility, cofomer lipophilicity (or partition coefficient,  $\log P$ ) is another crucial factor governing the membrane permeability of cocrystals.<sup>121–124</sup> NFT has a  $\log P$  value of  $-0.7$ ,<sup>125</sup> which indicates the hydrophilic nature of the drug. It was therefore expected that the 2AmBZA and 2OHBZA cofomers with higher  $\log P$  values (0.5 and 1.4, respectively) in comparison to those of iNA ( $\log P = -0.3$ ) and PicAm ( $\log P = 0$ ), would improve the NFT diffusion behavior. However, the expected effect of cofomer lipophilicity on NFT diffusion was not observed, since the NFT cocrystals undergo rapid SMPT in aqueous media and the components permeate independently through the membrane. Most probably, this is the reason for the similarity of the API flux in the [NFT-2OHBZA] and [NFT-2AmBZA] cocrystals and the parent NFT.

**3.6. Influence of Cocrystallization on NFT Photostability.** Exposing certain APIs to light can have devastating

effects that influence drug stability. The International Council for Harmonisation of Technical Requirements for Pharmaceuticals for Human Use (ICH) claims that photostability studies are an integral part of drug development.<sup>126</sup> Many drugs tend to decompose or undergo other structural changes induced by light during manufacturing, storage, and administration.<sup>127</sup> This can lead to a decrease in performance, unstable absorption, and undocumented side effects. Cocrystallization proves to be an effective strategy to prevent drug degradation on exposure to light.<sup>128,129</sup> For instance, NFT is prone to photoisomerization on a C=N double bond, leading to its decomposition into 5-nitro-2-furaldehyde and 1-aminohydantoin,<sup>130</sup> while NFT cocrystals have been reported to possess higher photostability in comparison to the original drug.<sup>40,41</sup>

In the present work, the photostability of nitrofurantoin cocrystals has also been studied. NFT and its cocrystals were distributed in watch glass aliquots and analyzed at various intervals of exposure under UV irradiation (1, 2, 4, 10, 25, 40, and 60 h). The photodegradation curves in Figure S11 clearly show that the new NFT cocrystals have enhanced photostability. According to the data obtained, the photostability of the systems under study decreases in the following order: [NFT-2OHBZA] (1:1) > [NFT-iNA] (1:1) > [NFT-PicAm] (1:1)  $\approx$  [NFT-2AmBZA] (1:1) > NFT. These results demonstrate that cocrystals exhibit significantly better photoprotection in comparison to NFT. It is worth noting that, in the present work, the UV emission range was 200–400 nm in comparison to 315–400 nm in the earlier studies by Vangala et al.<sup>40,41</sup> The extended range was considered, since it contained absorption maxima of NFT at both 265 and 367 nm. It was found that, after 60 h of the experiment, the concentration of the nitrofurantoin remaining in the studied cocrystals was 14–25% higher than that in the original API in comparison to the 6–12% increase in the previously studied systems<sup>40,41</sup> at the same exposure time. The increased photostability is probably associated with stronger intermolecular hydrogen bonds, which restrict the conformational freedom of the NFT molecule and prevent it from photoisomerization. These results are intermediate, and additional research is needed to fully understand the mechanism of the photostability increase. Thus, cocrystallization reduces the photoisomerization of the NFT molecule, which helps to reduce the degradation rate of the photosensitive nitrofurantoin and increase the drug shelf life.

## 4. CONCLUSIONS

This work provides a comprehensive description of the structural, thermodynamic, and solubility features of four novel pharmaceutical cocrystals of nitrofurantoin, an antibacterial drug, with isonicotinamide, picolinamide, 2-hydroxybenzamide, and 2-aminobenzamide. The single-crystal data complemented by a QTAIMC analysis allowed us to identify eight distinct supramolecular heterosynthons of hydrogen bonding in the studied crystals and to quantify their total interaction energies, with the cyclic imide–amide synthon being the most stable. Although the reported cocrystals contained no isostructural packing motifs and displayed a variety of heterosynthons, the persistent  $-N_{im}-H\cdots O=C-N_{amide}-H_2$  hydrogen bond between the NFT and cofomers was observed in all of the compounds and also appeared to be the strongest intermolecular interaction in the crystals. According to the thermodynamic parameters of cocrystal formation derived from solubility and solution calorimetry experiments, the cocrystallization reaction between NFT and iNA was entropy-driven.

The thermodynamic stability of the [NFT-PicAm] (1:1) and [NFT-2AmbZA] (1:1) cocrystals was primarily of enthalpic nature. In the case of [NFT-2OHBZA] (1:1), however, the obtained  $\Delta_{\text{form}}G^\circ$  and  $\Delta_{\text{form}}H^\circ$  values were not statistically different from zero. The computational studies provided a valuable insight into the origin of the low thermodynamic stability of [NFT-2OHBZA] (1:1), indicating that it was mainly due to the energetically unfavorable packing arrangement of this multicomponent structure, where the strongest donor in the 2OHBZA molecule and two acceptor atoms of NFT did not seem to be involved in any intermolecular interactions. It has been found that NFT cocrystallization with the selected cofomers can potentially increase the thermodynamic solubility of the drug in aqueous media from 3 to 15 times, depending on the pH and the cofomer used. However, the thermodynamic solubility advantage of the cocrystals was not translated into an enhanced dissolution performance due to the rapid solution-mediated phase transformation, suggesting that additional formulation strategies are required to inhibit fast particle surface precipitation of the drug during the dissolution and to prolong the expected supersaturation stage. Our preliminary permeability investigations showed that cocrystallization of NFT with 2OHBZA and 2AmbZA had a negligible effect on the drug diffusion through the lipophilic biomimetic membrane, while iNA and PicAm seemed to modulate the NFT diffusion behavior and flux. In addition, similarly to the multicomponent solid forms of NFT reported previously, all of the cocrystals described here demonstrated enhanced photostability in comparison to that of the parent drug.

## ■ ASSOCIATED CONTENT

### SI Supporting Information

The Supporting Information is available free of charge at <https://pubs.acs.org/doi/10.1021/acs.cgd.2c00044>.

Crystallographic data for the cocrystals, details of the CSD analysis, periodic DFT and MEP calculations, illustrations of packing projections for the NFT cocrystals and results of thermal analysis, experimental results of the solution calorimetry study and phase solubility diagrams, details of aqueous solubility studies (eutectic concentrations) and PXRD patterns of residual materials after dissolution experiments, and details of diffusion and photostability investigations (PDF)

### Accession Codes

CCDC 2131165–2131168 contain the supplementary crystallographic data for this paper. These data can be obtained free of charge via [www.ccdc.cam.ac.uk/data\\_request/cif](http://www.ccdc.cam.ac.uk/data_request/cif), or by emailing [data\\_request@ccdc.cam.ac.uk](mailto:data_request@ccdc.cam.ac.uk), or by contacting The Cambridge Crystallographic Data Centre, 12 Union Road, Cambridge CB2 1EZ, UK; fax: +44 1223 336033.

## ■ AUTHOR INFORMATION

### Corresponding Author

German L. Perlovich – G.A. Krestov Institute of Solution Chemistry RAS, 153045 Ivanovo, Russia; [orcid.org/0000-0002-6267-5244](https://orcid.org/0000-0002-6267-5244); Phone: +7-4932-533784; Email: [glp@isc-ras.ru](mailto:glp@isc-ras.ru); Fax: +7-4932- 336237

### Authors

Artem O. Surov – G.A. Krestov Institute of Solution Chemistry RAS, 153045 Ivanovo, Russia

Alexander P. Voronin – G.A. Krestov Institute of Solution Chemistry RAS, 153045 Ivanovo, Russia; [orcid.org/0000-0003-3881-2277](https://orcid.org/0000-0003-3881-2277)

Ksenia V. Drozd – G.A. Krestov Institute of Solution Chemistry RAS, 153045 Ivanovo, Russia; [orcid.org/0000-0001-9888-0648](https://orcid.org/0000-0001-9888-0648)

Tatyana V. Volkova – G.A. Krestov Institute of Solution Chemistry RAS, 153045 Ivanovo, Russia; [orcid.org/0000-0002-5841-2724](https://orcid.org/0000-0002-5841-2724)

Nikita Vasilev – G.A. Krestov Institute of Solution Chemistry RAS, 153045 Ivanovo, Russia

Dmitriy Batov – G.A. Krestov Institute of Solution Chemistry RAS, 153045 Ivanovo, Russia

Andrei V. Churakov – Institute of General and Inorganic Chemistry RAS, 119991 Moscow, Russia; [orcid.org/0000-0003-3336-4022](https://orcid.org/0000-0003-3336-4022)

Complete contact information is available at: <https://pubs.acs.org/doi/10.1021/acs.cgd.2c00044>

## Notes

The authors declare no competing financial interest.

## ■ ACKNOWLEDGMENTS

This work was supported by the Russian Science Foundation, Grant No. 19-73-10005. We also thank the “Upper Volga Region Centre of Physicochemical Research” for technical assistance with the PXRD and TGA experiments. The single-crystal X-ray diffraction studies were performed at the Centre of Shared Equipment of IGIC RAS.

## ■ REFERENCES

- (1) Kavanagh, O. N.; Croker, D. M.; Walker, G. M.; Zaworotko, M. J. Pharmaceutical cocrystals: from serendipity to design to application. *Drug Discovery Today* **2019**, *24*, 796–804.
- (2) Duggirala, N. K.; Perry, M. L.; Almarsson, Ö.; Zaworotko, M. J. Pharmaceutical cocrystals: along the path to improved medicines. *Chem. Commun.* **2016**, *52*, 640–655.
- (3) Bolla, G.; Nangia, A. Pharmaceutical cocrystals: walking the talk. *Chem. Commun.* **2016**, *52*, 8342–8360.
- (4) Berry, D. J.; Steed, J. W. Pharmaceutical cocrystals, salts and multicomponent systems; intermolecular interactions and property based design. *Adv. Drug Delivery Rev.* **2017**, *117*, 3–24.
- (5) Kuminek, G.; Cao, F.; Bahia de Oliveira da Rocha, A.; Gonçalves Cardoso, S.; Rodríguez-Hornedo, N. Cocrystals to facilitate delivery of poorly soluble compounds beyond-rule-of-5. *Adv. Drug Delivery Rev.* **2016**, *101*, 143–166.
- (6) Wong, S. N.; Chen, Y. C. S.; Xuan, B.; Sun, C. C.; Chow, S. F. Cocrystal engineering of pharmaceutical solids: therapeutic potential and challenges. *CrystEngComm* **2021**, *23*, 7005–7038.
- (7) Noonan, T. J.; Chibale, K.; Cheuka, P. M.; Bourne, S. A.; Caira, M. R. Cocrystal and Salt Forms of an Imidazopyridazine Antimalarial Drug Lead. *J. Pharm. Sci.* **2019**, *108*, 2349–2357.
- (8) Kimoto, K.; Yamamoto, M.; Karashima, M.; Hohokabe, M.; Takeda, J.; Yamamoto, K.; Ikeda, Y. Pharmaceutical Cocrystal Development of TAK-020 with Enhanced Oral Absorption. *Crystals* **2020**, *10*, 211.
- (9) Roy, P.; Ghosh, A. Progress on cocrystallization of poorly soluble NME's in the last decade. *CrystEngComm* **2020**, *22*, 6958–6974.
- (10) Walsh, R. D. B.; Bradner, M. W.; Fleischman, S.; Morales, L. A.; Moulton, B.; Rodríguez-Hornedo, N.; Zaworotko, M. J. Crystal engineering of the composition of pharmaceutical phases. *Chem. Commun.* **2003**, 186–187.
- (11) Mukherjee, A. Building upon Supramolecular Synthons: Some Aspects of Crystal Engineering. *Cryst. Growth Des.* **2015**, *15*, 3076–3085.

- (12) Corpinot, M. K.; Bućar, D.-K. A Practical Guide to the Design of Molecular Crystals. *Cryst. Growth Des.* **2019**, *19*, 1426–1453.
- (13) Desiraju, G. R. Supramolecular Synthons in Crystal Engineering—A New Organic Synthesis. *Angew. Chem., Int. Ed. Engl.* **1995**, *34*, 2311–2327.
- (14) Lemmerer, A.; Bernstein, J.; Kahlenberg, V. One-pot covalent and supramolecular synthesis of pharmaceutical co-crystals using the API isoniazid: a potential supramolecular reagent. *CrystEngComm* **2010**, *12*, 2856–2864.
- (15) Desiraju, G. R. Crystal Engineering: From Molecule to Crystal. *J. Am. Chem. Soc.* **2013**, *135*, 9952–9967.
- (16) Desiraju, G. R. Crystal Engineering: A Holistic View. *Angew. Chem., Int. Ed.* **2007**, *46*, 8342–8356.
- (17) Sun, L.; Wang, Y.; Yang, F.; Zhang, X.; Hu, W. Cocrystal Engineering: A Collaborative Strategy toward Functional Materials. *Adv. Mater.* **2019**, *31*, 1902328.
- (18) Schartman, R. R. On the thermodynamics of cocrystal formation. *Int. J. Pharm.* **2009**, *365*, 77–80.
- (19) Zhang, S.; Rasmuson, Å. C. Thermodynamics and Crystallization of the Theophylline-Glutamic Acid Cocrystal. *Cryst. Growth Des.* **2013**, *13*, 1153–1161.
- (20) Zhang, S.; Chen, H.; Rasmuson, Å. C. Thermodynamics and crystallization of a theophylline-salicylic acid cocrystal. *CrystEngComm* **2015**, *17*, 4125–4135.
- (21) Gavezzotti, A.; Colombo, V.; Lo Presti, L. Facts and Factors in the Formation and Stability of Binary Crystals. *Cryst. Growth Des.* **2016**, *16*, 6095–6104.
- (22) Taylor, C. R.; Day, G. M. Evaluating the Energetic Driving Force for Cocrystal Formation. *Cryst. Growth Des.* **2018**, *18*, 892–904.
- (23) Zhang, S.-W.; Brunskill, A. P. J.; Schwartz, E.; Sun, S. Celecoxib-Nicotinamide Cocrystal Revisited: Can Entropy Control Cocrystal Formation? *Cryst. Growth Des.* **2017**, *17*, 2836–2843.
- (24) Ahuja, D.; Svård, M.; Rasmuson, Å. C. Investigation of solid-liquid phase diagrams of the sulfamethazine-salicylic acid co-crystal. *CrystEngComm* **2019**, *21*, 2863–2874.
- (25) Svård, M.; Ahuja, D.; Rasmuson, Å. C. Calorimetric Determination of Cocrystal Thermodynamic Stability: Sulfamethazine-Salicylic Acid Case Study. *Cryst. Growth Des.* **2020**, *20*, 4243–4251.
- (26) Perlovich, G. L. Formation Thermodynamics of Two-Component Molecular Crystals: Polymorphism, Stoichiometry, and Impact of Enantiomers. *Cryst. Growth Des.* **2020**, *20*, 5526–5537.
- (27) Watari, N.; Funaki, T.; Aizawa, K.; Kaneniwa, N. Nonlinear assessment of nitrofurantoin bioavailability in rabbits. *J. Pharmacokinetics. Biopharm.* **1983**, *11*, 529–545.
- (28) Kons, A.; Mishnev, A.; Mukhametzyanov, T. A.; Buzyurov, A. V.; Lapuk, S. E.; Bērziņš, A. Hexamorphism of Dantrolene: Insight into the Crystal Structures, Stability, and Phase Transformations. *Cryst. Growth Des.* **2021**, *21*, 1190–1201.
- (29) Jarzemska, K. N.; Kubsik, M.; Kamiński, R.; Woźniak, K.; Dominiak, P. M. From a Single Molecule to Molecular Crystal Architectures: Structural and Energetic Studies of Selected Uracil Derivatives. *Cryst. Growth Des.* **2012**, *12*, 2508–2524.
- (30) Chennuru, R.; Muthudoss, P.; Voguri, R. S.; Ramakrishnan, S.; Vishweshwar, P.; Babu, R. R. C.; Mahapatra, S. Iso-Structurality Induced Solid Phase Transformations: A Case Study with Lenalidomide. *Cryst. Growth Des.* **2017**, *17*, 612–628.
- (31) Aitipamula, S.; Chow, P. S.; Tan, R. B. H. Crystal Engineering of Tegafur Cocrystals: Structural Analysis and Physicochemical Properties. *Cryst. Growth Des.* **2014**, *14*, 6557–6569.
- (32) Chatziadi, A.; Skořepová, E.; Rohlíček, J.; Dušek, M.; Ridvan, L.; Šoós, M. Mechanochemically Induced Polymorphic Transformations of Sofosbuvir. *Cryst. Growth Des.* **2020**, *20*, 139–147.
- (33) Bhatt, P. M.; Azim, Y.; Thakur, T. S.; Desiraju, G. R. Co-Crystals of the Anti-HIV Drugs Lamivudine and Zidovudine. *Cryst. Growth Des.* **2009**, *9*, 951–957.
- (34) Cherukuvada, S.; Babu, N. J.; Nangia, A. Nitrofurantoin-p-aminobenzoic acid cocrystal: Hydration stability and dissolution rate studies. *J. Pharm. Sci.* **2011**, *100*, 3233–3244.
- (35) Zhang, Z.; Cai, Q.; Xue, J.; Qin, J.; Liu, J.; Du, Y. Co-Crystal Formation of Antibiotic Nitrofurantoin Drug and Melamine Co-Former Based on a Vibrational Spectroscopic Study. *Pharmaceutics* **2019**, *11*, 56.
- (36) Maity, D. K.; Paul, R. K.; Desiraju, G. R. Drug-Drug Binary Solids of Nitrofurantoin and Trimethoprim: Crystal Engineering and Pharmaceutical Properties. *Mol. Pharmaceutics* **2020**, *17*, 4435–4442.
- (37) Kasim, N. A.; Whitehouse, M.; Ramachandran, C.; Bermejo, M.; Lennernäs, H.; Hussain, A. S.; Junginger, H. E.; Stavchansky, S. A.; Midha, K. K.; Shah, V. P.; Amidon, G. L. Molecular Properties of WHO Essential Drugs and Provisional Biopharmaceutical Classification. *Mol. Pharmaceutics* **2004**, *1*, 85–96.
- (38) Rosenberg, H. A.; Bates, T. R. The influence of food on nitrofurantoin bioavailability. *Clin. Pharmacol. Ther.* **1976**, *20*, 227–232.
- (39) Wijma, R. A.; Franssen, F.; Muller, A. E.; Mouton, J. W. Optimizing dosing of nitrofurantoin from a PK/PD point of view: What do we need to know? *Drug Resistance Updates* **2019**, *43*, 1–9.
- (40) Vangala, V. R.; Chow, P. S.; Tan, R. B. H. Characterization, physicochemical and photo-stability of a co-crystal involving an antibiotic drug, nitrofurantoin, and 4-hydroxybenzoic acid. *CrystEngComm* **2011**, *13*, 759–762.
- (41) Vangala, V. R.; Chow, P. S.; Tan, R. B. H. Co-Crystals and Co-Crystal Hydrates of the Antibiotic Nitrofurantoin: Structural Studies and Physicochemical Properties. *Cryst. Growth Des.* **2012**, *12*, 5925–5938.
- (42) Vangala, V. R.; Chow, P. S.; Tan, R. B. H. The solvates and salt of antibiotic agent, nitrofurantoin: structural, thermochemical and desolvation studies. *CrystEngComm* **2013**, *15*, 878–889.
- (43) Alhalaweh, A.; George, S.; Basavoju, S.; Childs, S. L.; Rizvi, S. A. A.; Velaga, S. P. Pharmaceutical cocrystals of nitrofurantoin: screening, characterization and crystal structure analysis. *CrystEngComm* **2012**, *14*, 5078–5088.
- (44) Sheldrick, G. *SADABS, Program for scaling and correction of area detector data*; University of Göttingen: 1997.
- (45) Sheldrick, G. A short history of SHELX. *Acta Crystallogr. Sect. A: Found. Crystallogr.* **2008**, *64*, 112–122.
- (46) Ivanov, E. V.; Batov, D. V. Unusual behavior of temperature-dependent solvent H/D isotope effects in the enthalpy and heat capacity of hexamethylenetetramine (urotropine) hydration. *J. Mol. Liq.* **2019**, *285*, 508–514.
- (47) Batov, D. V.; Antonova, O. A. Effect of structural isomerism of propanol or butanol molecules on their enthalpy of dissolution and solvation in water - Methanol mixtures. *J. Mol. Liq.* **2019**, *287*, 110962.
- (48) Ivanov, E. V.; Batov, D. V. Enthalpies and heat capacities of solution of racemic N-methyl-substituted glycolurils in water at T = (278.15 to 313.15)K. *Thermochim. Acta* **2015**, *620*, 59–64.
- (49) Dovesi, R.; Erba, A.; Orlando, R.; Zicovich-Wilson, C. M.; Civalieri, B.; Maschio, L.; Rérat, M.; Casassa, S.; Baima, J.; Salustro, S.; et al. Quantum-mechanical condensed matter simulations with CRYSTAL. *Wiley Interdisciplinary Reviews: Computational Molecular Science* **2018**, *8*, No. e1360.
- (50) Grimme, S.; Antony, J.; Ehrlich, S.; Krieg, H. A consistent and accurate ab initio parametrization of density functional dispersion correction (DFT-D) for the 94 elements H-Pu. *J. Chem. Phys.* **2010**, *132*, 154104.
- (51) Grimme, S.; Ehrlich, S.; Goerigk, L. Effect of the damping function in dispersion corrected density functional theory. *J. Comput. Chem.* **2011**, *32*, 1456–1465.
- (52) Becke, A. D. Density-functional thermochemistry. III. The role of exact exchange. *J. Chem. Phys.* **1993**, *98*, 5648–5652.
- (53) Vener, M. V.; Levina, E. O.; Koloskov, O. A.; Rykounov, A. A.; Voronin, A. P.; Tsirelson, V. G. Evaluation of the lattice energy of the two-component molecular crystals using solid-state density functional theory. *Cryst. Growth Des.* **2014**, *14*, 4997–5003.
- (54) Manin, A. N.; Voronin, A. P.; Drozd, K. V.; Perlovich, G. L. Thermodynamic properties of Nalidixic and Oxolinic acids: Experimental and computational study. *Thermochim. Acta* **2019**, *682*, 178411.

- (55) Surov, A. O.; Manin, A. N.; Voronin, A. P.; Boycov, D. E.; Magdysyuk, O. V.; Perlovich, G. L. New Pharmaceutical Cocrystal Forms of Flurbiprofen: Structural, Physicochemical, and Thermodynamic Characterization. *Cryst. Growth Des.* **2019**, *19*, 5751–5761.
- (56) Gatti, C.; Saunders, V. R.; Roetti, C. Crystal field effects on the topological properties of the electron density in molecular crystals: The case of urea. *J. Chem. Phys.* **1994**, *101*, 10686–10696.
- (57) Mata, I.; Alkorta, I.; Espinosa, E.; Molins, E. Relationships between interaction energy, intermolecular distance and electron density properties in hydrogen bonded complexes under external electric fields. *Chem. Phys. Lett.* **2011**, *507*, 185–189.
- (58) Vener, M. V.; Egorova, A. N.; Churakov, A. V.; Tsirelson, V. G. Intermolecular hydrogen bond energies in crystals evaluated using electron density properties: DFT computations with periodic boundary conditions. *J. Comput. Chem.* **2012**, *33*, 2303–2309.
- (59) Shishkina, A. V.; Zhurov, V. V.; Stash, A. I.; Vener, M. V.; Pinkerton, A. A.; Tsirelson, V. G. Noncovalent interactions in crystalline picolinic acid N-oxide: insights from experimental and theoretical charge density analysis. *Crystal Growth Design* **2013**, *13*, 816–828.
- (60) Vener, M. V.; Shishkina, A. V.; Rykounov, A. A.; Tsirelson, V. G. Cl & Cl interactions in molecular crystals: Insights from the theoretical charge density analysis. *J. Phys. Chem. A* **2013**, *117*, 8459–8467.
- (61) Manin, A. N.; Voronin, A. P.; Manin, N. G.; Vener, M. V.; Shishkina, A. V.; Lermontov, A. S.; Perlovich, G. L. Salicylamide Cocrystals: Screening, Crystal Structure, Sublimation Thermodynamics, Dissolution, and Solid-State DFT Calculations. *J. Phys. Chem. B* **2014**, *118*, 6803–6814.
- (62) Surov, A. O.; Churakov, A. V.; Perlovich, G. L. Three Polymorphic Forms of Ciprofloxacin Maleate: Formation Pathways, Crystal Structures, Calculations, and Thermodynamic Stability Aspects. *Crystal Growth Design* **2016**, *16*, 6556–6567.
- (63) Voronin, A. P.; Volkova, T. V.; Ilyukhin, A. B.; Trofimova, T. P.; Perlovich, G. L. Structural and energetic aspects of adamantane and memantine derivatives of sulfonamide molecular crystals: experimental and theoretical characterisation. *CrystEngComm* **2018**, *20*, 3476–3489.
- (64) Boys, S. F.; Bernardi, F. The calculation of small molecular interactions by the differences of separate total energies. Some procedures with reduced errors. *Mol. Phys.* **1970**, *19*, 553–566.
- (65) Surov, A. O.; Voronin, A. P.; Vener, M. V.; Churakov, A. V.; Perlovich, G. L. Specific features of supramolecular organisation and hydrogen bonding in proline cocrystals: a case study of fenamates and diclofenac. *CrystEngComm* **2018**, *20*, 6970–6981.
- (66) Murray, J. S.; Politzer, P. Hydrogen Bonding: A Coulombic  $\sigma$ -Hole Interaction. *Journal of the Indian Institute of Science* **2020**, *100*, 21–30.
- (67) Frisch, M. J.; Trucks, G. W.; Schlegel, H. B.; Scuseria, G. E.; Robb, M. A.; Cheeseman, J. R.; Scalmani, G.; Barone, V.; Mennucci, B.; Petersson, G. A.; Nakatsuji, H.; Caricato, M.; Li, X.; Hratchian, H. P.; Izmaylov, A. F.; Bloino, J.; Zheng, G.; Sonnenberg, J. L.; Hada, M.; Ehara, M.; Toyota, K.; Fukuda, R.; Hasegawa, J.; Ishida, M.; Nakajima, T.; Honda, Y.; Kitao, O.; Nakai, H.; Vreven, T.; Montgomery, J. A.; Peralta, J. E.; Ogliaro, F.; Bearpark, M.; Heyd, J. J.; Brothers, E.; Kudin, K. N.; Staroverov, V. N.; Kobayashi, R.; Normand, J.; Raghavachari, K.; Rendell, A.; Burant, J. C.; Iyengar, S. S.; Tomasi, J.; Cossi, M.; Rega, N.; Millam, J. M.; Klene, M.; Knox, J. E.; Cross, J. B.; Bakken, V.; Adamo, C.; Jaramillo, J.; Gomperts, R.; Stratmann, R. E.; Yazyev, O.; Austin, A. J.; Cammi, R.; Pomelli, C.; Ochterski, J. W.; Martin, R. L.; Morokuma, K.; Zakrzewski, V. G.; Voth, G. A.; Salvador, P.; Dannenberg, J. J.; Dapprich, S.; Daniels, A. D.; Farkas Foresman, J. B.; Ortiz, J. V.; Cioslowski, J.; Fox, D. J. *Gaussian 09, Rev. B.01*; Gaussian Inc.: 2009.
- (68) Lu, T.; Chen, F. Multiwfn: A multifunctional wavefunction analyzer. *J. Comput. Chem.* **2012**, *33*, 580–592.
- (69) Mapp, L. K.; Coles, S. J.; Aitipamula, S. Design of Cocrystals for Molecules with Limited Hydrogen Bonding Functionalities: Propyphenazone as a Model System. *Cryst. Growth Des.* **2017**, *17*, 163–174.
- (70) Manin, A. N.; Drozd, K. V.; Churakov, A. V.; Perlovich, G. L. Hydrogen Bond Donor/Acceptor Ratios of the Cofomers: Do They Really Matter for the Prediction of Molecular Packing in Cocrystals? The Case of Benzamide Derivatives with Dicarboxylic Acids. *Cryst. Growth Des.* **2018**, *18*, 5254–5269.
- (71) Alvarez-Lorenzo, C.; Castiñeiras, A.; Frontera, A.; García-Santos, I.; González-Pérez, J. M.; Niclós-Gutiérrez, J.; Rodríguez-González, I.; Vilchez-Rodríguez, E.; Zareba, J. K. Recurrent motifs in pharmaceutical cocrystals involving glycolic acid: X-ray characterization, Hirshfeld surface analysis and DFT calculations. *CrystEngComm* **2020**, *22*, 6674–6689.
- (72) Li, J.; Bourne, S. A.; Caira, M. R. New polymorphs of isonicotinamide and nicotinamide. *Chem. Commun.* **2011**, *47*, 1530–1532.
- (73) Eccles, K. S.; Deasy, R. E.; Fábian, L.; Braun, D. E.; Maguire, A. R.; Lawrence, S. E. Expanding the crystal landscape of isonicotinamide: concomitant polymorphism and co-crystallisation. *CrystEngComm* **2011**, *13*, 6923–6925.
- (74) Yan, Y.; Chen, J.-M.; Geng, N.; Lu, T.-B. Improving the Solubility of Agomelatine via Cocrystals. *Cryst. Growth Des.* **2012**, *12*, 2226–2233.
- (75) Domingos, S.; Fernandes, A.; Duarte, M. T.; Piedade, M. F. M. New Multicomponent Sulfadimethoxine Crystal Forms: Sulfonamides as Participants in Supramolecular Interactions. *Cryst. Growth Des.* **2016**, *16*, 1879–1892.
- (76) Báthori, N. B.; Lemmerer, A.; Venter, G. A.; Bourne, S. A.; Caira, M. R. Pharmaceutical Co-crystals with Isonicotinamide—Vitamin B3, Clofibrac Acid, and Diclofenac—and Two Isonicotinamide Hydrates. *Cryst. Growth Des.* **2011**, *11*, 75–87.
- (77) Etter, M. C. Encoding and decoding hydrogen-bond patterns of organic compounds. *Acc. Chem. Res.* **1990**, *23*, 120–126.
- (78) Etter, M. C. Hydrogen bonds as design elements in organic chemistry. *J. Phys. Chem.* **1991**, *95*, 4601–4610.
- (79) Voronin, A. P.; Perlovich, G. L.; Vener, M. V. Effects of the crystal structure and thermodynamic stability on solubility of bioactive compounds: DFT study of isoniazid cocrystals. *Computational and Theoretical Chemistry* **2016**, *1092*, 1–11.
- (80) Surov, A. O.; Solanko, K. A.; Bond, A. D.; Bauer-Brandl, A.; Perlovich, G. L. Cocrystals of the antiandrogenic drug bicalutamide: screening, crystal structures, formation thermodynamics and lattice energies. *CrystEngComm* **2016**, *18*, 4818–4829.
- (81) Surov, A. O.; Voronin, A. P.; Vasilev, N. A.; Churakov, A. V.; Perlovich, G. L. Cocrystals of Fluconazole with Aromatic Carboxylic Acids: Competition between Anhydrous and Hydrated Solid Forms. *Cryst. Growth Des.* **2020**, *20*, 1218–1228.
- (82) Liu, C.; Wang, C.; Wan, S.; Liu, L.; Sun, C. C.; Qian, F. An Elusive Drug-Drug Cocrystal Prepared Using a Heteroseeding Strategy. *Cryst. Growth Des.* **2021**, *21*, 5659–5668.
- (83) Nehm, S. J.; Rodríguez-Spong, B.; Rodríguez-Hornedo, N. Phase Solubility Diagrams of Cocrystals Are Explained by Solubility Product and Solution Complexation. *Cryst. Growth Des.* **2006**, *6*, 592–600.
- (84) Alhalaweh, A.; Sokolowski, A.; Rodríguez-Hornedo, N.; Velaga, S. P. Solubility Behavior and Solution Chemistry of Indomethacin Cocrystals in Organic Solvents. *Cryst. Growth Des.* **2011**, *11*, 3923–3929.
- (85) Ma, K.; Zhang, Y.; Kan, H.; Cheng, L.; Luo, L.; Su, Q.; Gao, J.; Gao, Y.; Zhang, J. Thermodynamic and Kinetic Investigation on the Crucial Factors Affecting Adefovir Dipivoxil-Saccharin Cocrystallization. *Pharm. Res.* **2014**, *31*, 1766–1778.
- (86) Good, D. J.; Rodríguez-Hornedo, N. Cocrystal Eutectic Constants and Prediction of Solubility Behavior. *Cryst. Growth Des.* **2010**, *10*, 1028–1032.
- (87) Kuminek, G.; Cavanagh, K. L.; Rodríguez-Hornedo, N., Measurement and Mathematical Relationships of Cocrystal Thermodynamic Properties. In *Pharmaceutical Crystals: Science and Engineering*; Li, T., Mattei, A., Eds.; Wiley: 2019.
- (88) Zhang, S.-W.; Harasimowicz, M. T.; de Villiers, M. M.; Yu, L. Cocrystals of Nicotinamide and (R)-Mandelic Acid in Many Ratios with Anomalous Formation Properties. *J. Am. Chem. Soc.* **2013**, *135*, 18981–18989.

- (89) Zhang, S.-W.; Guzei, I. A.; de Villiers, M. M.; Yu, L.; Krzyzaniak, J. F. Formation Enthalpies and Polymorphs of Nicotinamide-R-Mandelic Acid Co-Crystals. *Cryst. Growth Des.* **2012**, *12*, 4090–4097.
- (90) Duggirala, N. K.; Frericks Schmidt, H. L.; Lei, Z.; Zaworotko, M. J.; Krzyzaniak, J. F.; Arora, K. K. Solid-State Characterization and Relative Formation Enthalpies To Evaluate Stability of Cocrystals of an Antidiabetic Drug. *Mol. Pharmaceutics* **2018**, *15*, 1901–1908.
- (91) Évora, A. O. L.; Castro, R. A. E.; Maria, T. M. R.; Silva, M. R.; ter Horst, J. H.; Canotilho, J.; Eusébio, M. E. S. A thermodynamic based approach on the investigation of a diflunisal pharmaceutical co-crystal with improved intrinsic dissolution rate. *Int. J. Pharm.* **2014**, *466*, 68–75.
- (92) Surov, A. O.; Solanko, K. A.; Bond, A. D.; Bauer-Brandl, A.; Perlovich, G. L. Polymorphism of felodipine co-crystals with 4,4'-bipyridine. *CrystEngComm* **2014**, *16*, 6603–6611.
- (93) de Araujo, G. L. B.; Ferreira, F. F.; Bernardes, C. E. S.; Sato, J. A. P.; Gil, O. M.; de Faria, D. L. A.; Loebenberg, R.; Byrn, S. R.; Ghisleni, D. D. M.; Bou-Chacra, N. A.; Pinto, T. J. A.; Antonio, S. G.; Ferraz, H. G.; Zemlyanov, D.; Gonçalves, D. S.; Minas da Piedade, M. E. A New Thermodynamically Favored Flubendazole/Maleic Acid Binary Crystal Form: Structure, Energetics, and in Silico PBPK Model-Based Investigation. *Cryst. Growth Des.* **2018**, *18*, 2377–2386.
- (94) Évora, A. O. L.; Bernardes, C. E. S.; Piedade, M. F. M.; Conceição, A. C. L.; Minas da Piedade, M. E. Energetics of Glycine Cocrystal or Salt Formation with Two Regioisomers: Fumaric Acid and Maleic Acid. *Cryst. Growth Des.* **2019**, *19*, 5054–5064.
- (95) Feliciano, I. O.; Silva, D. P.; Piedade, M. F. M.; Bernardes, C. E. S.; Minas da Piedade, M. E. First and Second Dissociation Enthalpies in Bi-Component Crystals Consisting of Maleic Acid and L-Phenylalanine. *Molecules* **2021**, *26*, 5714.
- (96) Rapeenun, P.; Rarey, J.; Flood, A. E. Shortcut Method for the Prediction of the Cocrystal Solubility Line. *Cryst. Growth Des.* **2021**, *21*, 5534–5543.
- (97) Pal, S. Mixing Effects on the Ternary Phase Diagram of Cocrystals and Gibbs Formation Energy Calculation. *Cryst. Growth Des.* **2021**, *21*, 249–259.
- (98) Good, D. J.; Rodríguez-Hornedo, N. Solubility Advantage of Pharmaceutical Cocrystals. *Cryst. Growth Des.* **2009**, *9*, 2252–2264.
- (99) Huang, N.; Rodríguez-Hornedo, N. Engineering cocrystal thermodynamic stability and eutectic points by micellar solubilization and ionization. *CrystEngComm* **2011**, *13*, 5409–5422.
- (100) Huang, Y.; Kuminek, G.; Roy, L.; Cavanagh, K. L.; Yin, Q.; Rodríguez-Hornedo, N. Cocrystal Solubility Advantage Diagrams as a Means to Control Dissolution, Supersaturation, and Precipitation. *Mol. Pharmaceutics* **2019**, *16*, 3887–3895.
- (101) Babu, N. J.; Nangia, A. Solubility Advantage of Amorphous Drugs and Pharmaceutical Cocrystals. *Cryst. Growth Des.* **2011**, *11*, 2662–2679.
- (102) Otori, M.; Watanabe, T.; Uekusa, T.; Oki, J.; Inoue, D.; Sugano, K. Effects of Cofomer and Polymer on Particle Surface Solution-Mediated Phase Transformation of Cocrystals in Aqueous Media. *Mol. Pharmaceutics* **2020**, *17*, 3825–3836.
- (103) Jasani, M. S.; Kale, D. P.; Singh, I. P.; Bansal, A. K. Influence of Drug-Polymer Interactions on Dissolution of Thermodynamically Highly Unstable Cocrystal. *Mol. Pharmaceutics* **2019**, *16*, 151–164.
- (104) Hu, C.; Liu, Z.; Liu, C.; Li, J.; Wang, Z.; Xu, L.; Chen, C.; Fan, H.; Qian, F. Enhanced Oral Bioavailability and Anti-Echinococcosis Efficacy of Albendazole Achieved by Optimizing the “Spring” and “Parachute”. *Mol. Pharmaceutics* **2019**, *16*, 4978–4986.
- (105) Remenar, J. F.; Peterson, M. L.; Stephens, P. W.; Zhang, Z.; Zimenkov, Y.; Hickey, M. B. Celecoxib:Nicotinamide Dissociation: Using Excipients To Capture the Cocrystal's Potential. *Mol. Pharmaceutics* **2007**, *4*, 386–400.
- (106) Guo, M.; Wang, K.; Hamill, N.; Lorimer, K.; Li, M. Investigating the Influence of Polymers on Supersaturated Flufenamic Acid Cocrystal Solutions. *Mol. Pharmaceutics* **2016**, *13*, 3292–3307.
- (107) Guo, M.; Wang, K.; Qiao, N.; Yardley, V.; Li, M. Investigating Permeation Behavior of Flufenamic Acid Cocrystals Using a Dissolution and Permeation System. *Mol. Pharmaceutics* **2018**, *15*, 4257–4272.
- (108) Salas-Zúñiga, R.; Rodríguez-Ruiz, C.; Höpfl, H.; Morales-Rojas, H.; Sánchez-Guadarrama, O.; Rodríguez-Cuamatzi, P.; Herrera-Ruiz, D. Dissolution Advantage of Nitazoxanide Cocrystals in the Presence of Cellulosic Polymers. *Pharmaceutics* **2020**, *12*, 23.
- (109) Wang, C.; Tong, Q.; Hou, X.; Hu, S.; Fang, J.; Sun, C. C. Enhancing Bioavailability of Dihydropyridinone through Inhibiting Precipitation of Soluble Cocrystals by a Crystallization Inhibitor. *Cryst. Growth Des.* **2016**, *16*, 5030–5039.
- (110) Feng, Y.; Meng, Y.; Tan, F.; Lv, L.; Li, Z.; Wang, Y.; Yang, Y.; Gong, W.; Yang, M. Effect of Surfactants and Polymers on the Dissolution Behavior of Supersaturable Tecovirimat-4-Hydroxybenzoic Acid Cocrystals. *Pharmaceutics* **2021**, *13*, 1772.
- (111) Kuminek, G.; Rodríguez-Hornedo, N.; Siedler, S.; Rocha, H. V. A.; Cuffini, S. L.; Cardoso, S. G. How cocrystals of weakly basic drugs and acidic cofomers might modulate solubility and stability. *Chem. Commun.* **2016**, *52*, 5832–5835.
- (112) Thakuria, R.; Delori, A.; Jones, W.; Lipert, M. P.; Roy, L.; Rodríguez-Hornedo, N. Pharmaceutical cocrystals and poorly soluble drugs. *Int. J. Pharm.* **2013**, *453*, 101–125.
- (113) Chen, Y. M.; Rodríguez-Hornedo, N. Cocrystals Mitigate Negative Effects of High pH on Solubility and Dissolution of a Basic Drug. *Cryst. Growth Des.* **2018**, *18*, 1358–1366.
- (114) Kuminek, G.; Cavanagh, K. L.; da Piedade, M. F. M.; Rodríguez-Hornedo, N. Posaconazole Cocrystal with Superior Solubility and Dissolution Behavior. *Cryst. Growth Des.* **2019**, *19*, 6592–6602.
- (115) Childs, S. L.; Kandi, P.; Lingireddy, S. R. Formulation of a Danazol Cocrystal with Controlled Supersaturation Plays an Essential Role in Improving Bioavailability. *Mol. Pharmaceutics* **2013**, *10*, 3112–3127.
- (116) Alhalaweh, A.; Ali, H. R. H.; Velaga, S. P. Effects of Polymer and Surfactant on the Dissolution and Transformation Profiles of Cocrystals in Aqueous Media. *Cryst. Growth Des.* **2014**, *14*, 643–648.
- (117) Guo, M.; Wang, K.; Qiao, N.; Fábian, L.; Sadiq, G.; Li, M. Insight into Flufenamic Acid Cocrystal Dissolution in the Presence of a Polymer in Solution: from Single Crystal to Powder Dissolution. *Mol. Pharmaceutics* **2017**, *14*, 4583–4596.
- (118) Otori, M.; Uekusa, T.; Oki, J.; Inoue, D.; Sugano, K. Solution-mediated phase transformation at particle surface during cocrystal dissolution. *J. Drug Delivery Sci. Technol.* **2020**, *56*, 101566.
- (119) Costa, P.; Sousa Lobo, J. M. Modeling and comparison of dissolution profiles. *Eur. J. Pharm. Sci.* **2001**, *13*, 123–133.
- (120) Shah, V. P.; Amidon, G. L.; Lennernas, H.; Crison, J. R. A Theoretical Basis for a Biopharmaceutic Drug Classification: The Correlation of In Vitro Drug Product Dissolution and In Vivo Bioavailability. *AAPS Journal* **2014**, *16*, 894–898.
- (121) Yan, Y.; Chen, J.-M.; Lu, T.-B. Simultaneously enhancing the solubility and permeability of acyclovir by crystal engineering approach. *CrystEngComm* **2013**, *15*, 6457–6460.
- (122) Suzuki, Y.; Muangnoi, C.; Thaweest, W.; Teerawonganan, P.; Ratnatilaka Na Bhuket, P.; Titapiwatanakun, V.; Yoshimura-Fujii, M.; Sritularak, B.; Likhitwitayawuid, K.; Rojsitthisak, P.; Fukami, T. Exploring Novel Cocrystalline Forms of Oxycodone to Enhance Aqueous Solubility and Permeability across a Cell Monolayer. *Biol. Pharm. Bull.* **2019**, *42*, 1004–1012.
- (123) Ji, X.; Wu, D.; Li, C.; Li, J.; Sun, Q.; Chang, D.; Yin, Q.; Zhou, L.; Xie, C.; Gong, J.; Chen, W. Enhanced Solubility, Dissolution, and Permeability of Abacavir by Salt and Cocrystal Formation. *Cryst. Growth Des.* **2022**, *22*, 428.
- (124) Palanisamy, V.; Sanphui, P.; Jyothi, V. G. S. S.; Shastri, N. R.; Bolla, G.; Palanisamy, K.; Prakash, M.; Vangala, V. R. Tuning Diffusion Permeability of an Anti-Retroviral Drug, Emtricitabine, via Multi-component Crystallizations. *Cryst. Growth Des.* **2021**, *21*, 1548–1561.
- (125) Kallinteri, P.; G. Antimisariis, S. Solubility of drugs in the presence of gelatin: effect of drug lipophilicity and degree of ionization. *Int. J. Pharm.* **2001**, *221*, 219–226.

(126) Drug Quality Q1B: Photostability testing of new drug substance and products. In ed.; *ICH Harmonized Tripartite Guideline: US FDA*: 1996; Vol. 62, pp 27115–27122.

(127) Tonnesen, H. H. *Photostability of drugs and drug formulations*. ed.; CRC Press: 2004.

(128) Putra, O. D.; Umeda, D.; Nugraha, Y. P.; Nango, K.; Yonemochi, E.; Uekusa, H. Simultaneous Improvement of Epalrestat Photostability and Solubility via Cocrystallization: A Case Study. *Cryst. Growth Des.* **2018**, *18*, 373–379.

(129) SeethaLekshmi, S.; Thakur, T. S.; Varughese, S. Photoinstability in active pharmaceutical ingredients: Crystal engineering as a mitigating measure. *Journal of Photochemistry and Photobiology C: Photochemistry Reviews* **2021**, *49*, 100455.

(130) Szabó-Bárdos, E.; Cafuta, A.; Hegedás, P.; Fónagy, O.; Kiss, G.; Babić, S.; Škorić, I.; Horváth, O. Photolytic and photocatalytic degradation of nitrofurantoin and its photohydrolytic products. *J. Photochem. Photobiol., A* **2020**, *386*, 112093.

**JACS Au**  
AN OPEN ACCESS JOURNAL OF THE AMERICAN CHEMICAL SOCIETY

Editor-in-Chief  
**Prof. Christopher W. Jones**  
Georgia Institute of Technology, USA

**Open for Submissions**

pubs.acs.org/jacsau

ACS Publications  
Most Trusted. Most Cited. Most Read.